

1 **Imprint of minute hydrocarbon seepage on solid phase and pore water**  
2 **geochemistry in organic-poor subseafloor sediment**

3 Ellen Schnabel<sup>1\*</sup>, Jessica Stammeier<sup>2</sup>, Stefanie Poetz<sup>3</sup>, Kai Mangelsdorf<sup>3</sup>, Aurèle Vuillemin<sup>1</sup>,  
4 Rolando di Primio<sup>4</sup>, Jens Kallmeyer<sup>1</sup>, the PROSPECTOMICS Consortium

5 <sup>1</sup>GFZ Helmholtz Centre for Geosciences, Section Geomicrobiology, Telegrafenberg, 14473  
6 Potsdam, Germany

7 <sup>2</sup>GFZ Helmholtz Centre for Geosciences, Section Inorganic and Isotope Geochemistry,  
8 Telegrafenberg, 14473 Potsdam, Germany

9 <sup>3</sup>GFZ Helmholtz Centre for Geosciences, Section Organic Geochemistry, Telegrafenberg,  
10 14473 Potsdam, Germany

11 <sup>4</sup>AkerBP, 1366 Lysaker, Norway

12 \*Corresponding author: MSc Ellen Schnabel, eschnabe@gfz.de

13 Keywords: hydrocarbon seepage; reductive diagenesis; authigenic minerals; microbial  
14 activity; Barents Sea; sediment biogeochemistry

15 **Key Points**

- 16 • Even inconspicuous hydrocarbon seepage modifies redox zonation and stimulates  
17 carbonate and sulfide mineral formation in marine sediments.
- 18 • Subtle seepage causes distinct spatial heterogeneity in pore water chemistry and  
19 mineral formation patterns.
- 20 • Authigenic minerals and pore water gradients serve as complementary indicators of  
21 past and ongoing seepage.

22 **Abstract**

23 In marine environments, small hydrocarbon (HC) fluxes through organic-poor sediments are  
24 often fully degraded by microorganisms before reaching the seabed. Yet, these fluxes  
25 influence sediment geochemistry by stimulating microbial activity. We analyzed 50 gravity  
26 cores from the southwestern Barents Sea, covering zones affected by inconspicuous HC  
27 seepage and unaffected reference zones. Using various organic and inorganic geochemical

28 analyses of the sediment along with pore water geochemistry, we assess the effects of low-  
29 intensity seepage and identify potential geochemical signatures.

30 While analysis of the organic geochemical analyses provided limited insights, inorganic  
31 geochemical analyses revealed formation of minerals such as carbonates and sulfides, linked  
32 to microbial reductive processes. Element concentrations suggested that HC degradation  
33 leaves distinct signatures, particularly in redox-sensitive minerals. Pore water profiles in HC-  
34 affected zones showed significant variation, indicating carbonate precipitation. In contrast,  
35 sediments not affected by HC seepage displayed more uniform pore water profiles.

36 Estimated fluxes of sulfate, calcium, and alkalinity varied notably between cores, particularly  
37 in HC-affected zones, suggesting local and potentially transient differences in seepage  
38 intensity.

39 While microbial HC degradation likely occurs deeper than our sampling interval, high-  
40 resolution geochemical analysis of both sediment fractions and pore water revealed a clear  
41 imprint of HC seepage. This imprint, reflected in authigenic minerals and pore water  
42 gradients, allows identification of past and present seepage activity, with authigenic  
43 minerals providing evidence for past seepage, and pore water profiles informing about  
44 ongoing seepage.

#### 45 **Plain language summary**

46 Hydrocarbons like methane or oil can naturally seep from underground reservoirs into  
47 marine sediments. Often, this seepage is so small that hydrocarbons are fully degraded by  
48 microorganisms before they reach the upper sediment layers near the seafloor.

49 In this study, we analyzed sediment from the southwestern Barents Sea, a region with very  
50 low natural organic content, to investigate whether such subtle hydrocarbon seepage leaves  
51 detectable traces, even when hydrocarbons are already consumed below the depth we  
52 sampled.

53 Our results show that despite the complete degradation of hydrocarbons deeper in the  
54 sediment, distinct changes in pore water chemistry and mineral composition persist in the  
55 upper layers. We observed variations in sulfate, calcium, and alkalinity profiles, along with  
56 the formation of minerals like carbonates and sulfides.

57 These findings reveal that even low-intensity hydrocarbon seepage can leave a long-lasting  
58 imprint in sediments, not only through direct hydrocarbon presence, but also through their  
59 impact on geochemical processes. This insight helps improving the detection of past or  
60 ongoing seepage in marine environments and supports a better understanding of  
61 biogeochemical cycles below the seafloor.

## 62 **1. Introduction**

63 Marine subseafloor biogeochemical cycles are primarily governed by microorganisms (Joye  
64 et al., 2022), their metabolic activity is strongly controlled by availability and reactivity of  
65 sedimentary organic substrates. Due to lesser primary productivity of surface waters as  
66 compared to coastal areas (Chavez et al., 2011), in offshore sediments bioavailable organic  
67 matter (OM) is typically limited and becomes more recalcitrant with burial depth  
68 (Middelburg, 2018) due to lower sedimentation rates (Røy et al., 2012). However, as all  
69 hydrocarbon reservoirs leak to some degree (Hunt, 1995; Heggland, 1998; Yergin, 2009),  
70 underlying hydrocarbon reservoirs will lead to buoyant hydrocarbon-rich fluids migrating  
71 upwards through the sediment column (Ciotoli et al., 2020). These HCs, even in trace  
72 amounts, represent an additional electron donor that can significantly fuel microbial activity  
73 (Zhang et al., 2022). Such influx of labile OM (i.e. seepage) leads to changes in microbial  
74 communities in terms of diversity and activity, which affect in turn specific physicochemical  
75 properties of the sediment, such as porosity, density, pore water geochemistry and mineral  
76 composition, (Abrams, 2005; Hvoslef et al., 1996; Joye, 2020). HC seepage through marine  
77 sediments fuels a variety of microbial processes, including sulfate reduction, fermentation,  
78 and methanogenesis (Joye, 2020; Schnabel et al., 2025). Although these microbial processes  
79 are central to *in situ* biogeochemical transformations of OM on the continental shelf  
80 (Bradley et al., 2020), they are less pronounced in pelagic sediments wherein sulfate  
81 reduction becomes limited due to energy limitation (Vuillemin et al., 2020). Thus, at sites  
82 with low seepage rates HCs may be fully mineralized before reaching the sediment surface.  
83 Nevertheless, subtle but continuous HC fluxes influence sediment geochemistry and  
84 microbiology, not only in the direct vicinity of the HC source but also extending to the  
85 sediment surface (Rasheed et al., 2013; Joye et al., 2004).

86 Dissimilatory sulfate reduction (DSR), which is the predominant terminal electron-accepting  
87 pathway in oxygen-depleted, sulfate-containing shallow marine sediments (Kasten and  
88 Jørgensen, 2000; Bowles et al., 2014; Jørgensen et al., 2019), can be expected to be  
89 influenced by HC seepage and potentially be key in defining HC-related reductive diagenesis  
90 (Joye et al., 2004). Organoclastic sulfate reduction (OSR) relies on low molecular weight  
91 substrates derived from fermented particulate or dissolved OM (Jørgensen, 1982), whereas  
92 methanotrophic sulfate reduction is performed in conjunction with methane-oxidizing  
93 archaea (ANME) during anaerobic oxidation of methane (AOM) (Orphan et al., 2001). Thus,  
94 the influence of HC seepage on sulfate-reducing bacteria (Widdel et al., 2010) highly  
95 depends on whether light (i.e. gaseous, soluble) or heavy (i.e. long chain alkanes, aromatic  
96 rings) HCs are supplied. The types of seeping HCs and their subsequent microbial alteration  
97 can be resolved using mass spectrometry of sediment organic extracts, e.g. a shift from  
98 polar to less polar unsaturated HCs is observed during maturation (Hu et al., 2023), whereas  
99 the loss of hydrogen atoms in alkanes (via dehydrogenation) or oxygen incorporation in  
100 aromatic rings (cleavage via hydroxylation) reveal subsequent microbial alteration (Sert et  
101 al., 2020). Further geochemical effects inherent to sulfate reduction (SR) include an increase  
102 in pore water alkalinity, primarily as dissolved inorganic carbon (DIC) in the form of  
103 bicarbonate ( $\text{HCO}_3^-$ ), and production of hydrogen sulfide ( $\text{H}_2\text{S}$ ). Together these metabolic  
104 solutes create favorable sedimentary conditions for the precipitation of carbonate and  
105 sulfide minerals (Berner, 1981; Hinrichs et al., 1999; Lin et al., 2016), namely calcite ( $\text{CaCO}_3$ ),  
106 mackinawite (FeS) and pyrite ( $\text{FeS}_2$ ). Carbonates can record redox conditions at the time of  
107 formation (Vuillemin et al., 2023a and 2023b) while their trace element compositions can  
108 indicate progressive alteration or diagenesis (Smrzka et al., 2019), in particular redox-  
109 sensitive trace metals (Smrzka et al., 2020; Tribovillard et al., 2013). Similarly, iron sulfides  
110 scavenge specific trace elements from the pore water (Huerta-Diaz and Morse, 1992),  
111 including chalcophilic and redox-sensitive bioessential metals (e.g., Mn, Mo, Cu, Zn).

112 Local redox conditions mediated by microbial processes also affect HC mobility as they  
113 promote the formation (e.g. carbonates) or dissolution (e.g. clays) of mineral barriers that  
114 adsorb HCs or impede their diffusion (Zhao et al., 2024; Eichhubl et al., 2009). For instance,  
115 the transition of smectite to illite decreases the mineral swelling capacity and reduces  
116 permeability (Kim et al., 2004; Dong et al., 2009). Such interplay of physical, geochemical

117 and biological factors affects the migration of HCs and generates complex but characteristic  
 118 flow patterns at active seep systems (De Groot et al., 2024). Thus, seep systems are  
 119 characterized by pronounced spatial and temporal variations, permeability, fluid flow  
 120 dynamics, and pressure conditions governing the rate at which HCs migrate upward (Foster  
 121 et al., 2015; Leifer et al., 2004; De Groot et al., 2024), reasons for which characteristic HC  
 122 seeps can be classified according to flux and surface manifestations (Table 1). Note that  
 123 some seep-features like e.g. carbonate crusts or pockmarks remain even after active  
 124 seepage stopped (Nickel et al. 2012, Nickel et al. 2013).

125 **Table 1.** Classification of hydrocarbon seeps based on methane flux and associated surface manifestations. The  
 126 table is compiled after (Judd and Hovland (2009); Etiope (2015)). The flux range between inconspicuous- and  
 127 moderate-flux seeps ( $1 \text{ mmol} \times \text{m}^2 \times \text{d}^{-1}$  to  $100 \text{ mmol} \times \text{m}^2 \times \text{d}^{-1}$ ) represents a conceptual transition zone,  
 128 where current data are insufficient to establish a clear distinction.

Seep type	Inconspicuous seeps	Moderate seeps	High flux seeps
Flux range	$< 1 \text{ mmol} \times \text{m}^2 \times \text{d}^{-1}$	$0.1\text{--}1 \text{ mol} \times \text{m}^2 \times \text{d}^{-1}$	$1\text{--}10 \text{ mol} \times \text{m}^2 \times \text{d}^{-1}$
Pockmarks	No pockmarks	Small, less deeply pronounced pockmarks	Larger, deeper and more numerous pockmarks, clearer
Methane and gas bubbles	No bubbles	Few, smaller bubbles, mostly sporadic	Frequent and larger bubbles, continuous gas flow
Chemical changes	No or minimal chemical changes on the surface	Low concentration of carbonates and sulfides	Significant enrichment of carbonates and sulfides, possible mineral deposits
Biogenic hotspots	No biological hotspots	Local colonization of methane-oxidizing bacteria	Intensive biological activity, larger hotspots with more diverse methane-fed fauna (e.g. mussels)
Gas hydrates	No gas hydrates	Little or no gas hydrates	Possible presence of gas hydrates, especially at low temperatures and high methane flow

129 According to our definition inconspicuous HC seeps are seeps where the seeping HCs lack  
130 visible surface manifestations. Instead, the HCs spread diffusely and are used up by  
131 biogeochemical processes so that the HCs do not reach the SWI. Although they likely imprint  
132 sediment geochemistry, they often remain undetected. Yet, any additional energy flux from  
133 weak seepage tends to promote complex interactions among local microbial communities  
134 adapted to substrate limitation or not, and influence the sediment geochemical dynamics,  
135 leading to fundamental metabolic and diagenetic processes (Abrams, 2020).

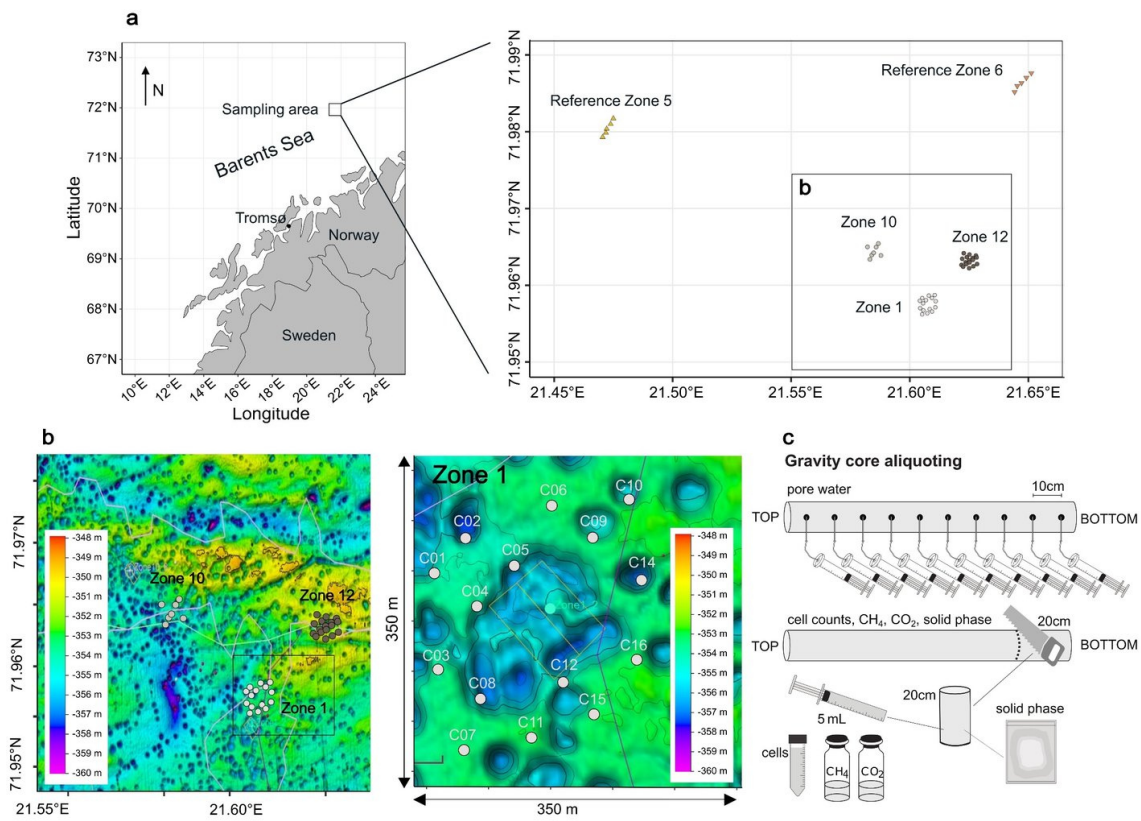
136 Here, we investigate how subtle, inconspicuous HC seepage influences the geochemical  
137 composition of both pore water and sediment. We analyzed 50 gravity cores collected from  
138 the southwestern Barents Sea, including 40 cores from zones affected by low-intensity  
139 seepage and 10 from unaffected reference zones. Given the challenges of deeper coring and  
140 the goal of minimizing environmental impact, we focused on the upper 3 meters of  
141 sediment to determine whether direct or indirect effects of seepage could be detected. The  
142 large number of cores allows us to identify small-scale geochemical patterns and evaluate  
143 any spatial heterogeneity of discrete infiltrations. By combining organic and inorganic  
144 analyses of the sediment with pore water geochemistry, we decipher (I) the extent to which  
145 inconspicuous HC seeps affect the distribution of key geochemical species (e.g. sulfide,  
146 methane, calcium, alkalinity) in pore water and sediment, and (II) how these parameters  
147 vary spatially across and between seepage and reference zones.

## 148 **2. Material and Methods**

### 149 **2.1. Geological setting and sampling**

150 The Barents Sea is an epicontinental shelf sea bordered by the Norwegian Sea to the  
151 southwest, the Arctic Ocean to the north, and the Russian archipelago of Novaya Zemlya to  
152 the east. It rests on a Caledonian basement formed during Paleozoic orogenies, but its  
153 present structural configuration mainly reflects Mesozoic and Cenozoic tectonic phases,  
154 including episodes of uplift, subsidence, tilting, and erosion. This has resulted in a varied  
155 structural landscape with elevated highs (e.g., the Loppa High) and intervening sedimentary  
156 basins (Doré, 1995; Gabrielsen et al., 1990; Johansen et al., 1993; Larssen et al., 2002;  
157 Faleide et al., 1984). During the Mesozoic, organic-rich marine shales were deposited under

158 greenhouse climate conditions with high marine productivity and fluctuating sea levels.  
 159 These shales—particularly the Upper Jurassic Hekkingen Formation, act as the principal  
 160 source rocks for hydrocarbons in the southwestern Barents Sea (Marín et al., 2020; Langrock  
 161 et al., 2003). Burial over millions of years led to thermal maturation, hydrocarbon  
 162 generation, and subsequent migration into structural traps, such as those found in the  
 163 Johan Castberg and Snøhvit fields. In the Quaternary, the region was repeatedly covered by  
 164 ice sheets. During the last glaciation, the Barents Sea was overridden by grounded ice,  
 165 leading to significant glacial erosion. Consequently, the modern sediment cover on  
 166 structural highs is often very thin and sediments primarily consist of glacial and glaciomarine  
 167 silty clays, dropstones, and fine sands derived from the erosion of local and distal bedrock  
 168 during glacial advance and retreat. These surficial sediments are typically organic-poor,  
 169 reflecting both their glacial origin and limited biological productivity during deposition  
 170 (Knies and Martinez, 2009; Nickel et al., 2013; Sættem et al. (1991); Elverhøi and Solheim  
 171 (1983).



172  
 173 **Figure 1. Sampling locations.** (a) Map of the Norwegian coast. The square marks the sampling area. Fifty cores  
 174 were retrieved from three HC-affected zones (Zone 1, Zone 10, Zone 12) and two reference zones (Ref 5, Ref  
 175 6). (b) Bathymetric map of the 3 HC-affected zones. Each zone was sampled in a grid of cores, Zone 1 is

176 enlarged here as an example. The missing samples in the middle are due to the increased occurrence of  
 177 dropstones in this area, preventing the deployment of a gravity corer. (c) Schematic overview of the sampling  
 178 strategy. This figure was modified after (Schnabel et al., 2025)

179 During an expedition to the SW Barents Sea in Oct/Nov 2021, we collected a total of fifty  
 180 gravity cores, ranging from 0.5 to 3 meters in length, within three zones with known  
 181 underlying HC reservoirs (Z01, Z10, Z12), as well as two zones (Ref5, Ref6) with no HC  
 182 reservoirs, labelled hereafter as HC zones and reference zones (Fig. 1a). The coring sites lie  
 183 at a water depth of approximately 350 meters (Fig. 1b). Immediately after retrieval of a  
 184 core (Fig. 1c), the lowermost 20 cm of the core were cut off, the sediment was pushed out  
 185 of the liner and the outer 1-2 cm were scraped off with a sterile spatula to remove possible  
 186 contamination. Using 5 mL cut-off syringes, 3 cm<sup>3</sup> of sediment were transferred into a 10 mL  
 187 glass crimp vial containing saturated NaCl solution. The vials were immediately sealed with  
 188 thick butyl rubber stoppers, crimped, and stored upside down without headspace until gas  
 189 analyses in the home lab. An additional 2 cm<sup>3</sup> of sediment was transferred into a 15 mL  
 190 centrifuge tube containing 8 mL of NaCl-formalin fixative solution (25 g × L<sup>-1</sup> NaCl, 20 g × L<sup>-1</sup>  
 191 formalin) and thoroughly homogenized for cell counting. The remaining sediment was  
 192 aliquoted for solid phase geochemistry. The rest of the core was cut into 1 m sections,  
 193 capped and stored on deck, as air, water and sediment temperature were all around 5 °C.

194 Pore water was extracted on board, with extractions initiated within two hours of core  
 195 retrieval. Rhizon pore water samplers (Rhizosphere Research Products B.V., Netherlands;  
 196 (Seeberg-Elverfeldt et al., 2005)) were inserted into the intact sediment core through small  
 197 holes drilled in ca. 10 cm intervals. Pore water collection took between 12 and 24 hours. The  
 198 collected pore water samples were 0.22 µm- filtered (Merck Millex™-GS Sterile Syringe Filter  
 199 Unit, MCE) and aliquoted for different downstream analyses. For anion, cation, and trace  
 200 element measurements, 1.5 mL each was collected in plastic screw-cap vials without any  
 201 further treatment. These samples were kept anoxic until analysis. For alkalinity  
 202 measurements, 2 mL of pore water were filled into a glass vial pre-filled with 50 µL of  
 203 saturated HgCl<sub>2</sub> solution to prevent bacterial activity (Edenborn et al., 1985) and closed  
 204 without any headspace. For quantification of dissolved hydrogen sulfide, we transferred 1.5  
 205 mL of pore water into a 2 mL plastic screw-cap vial and added 200 µL ZnCl<sub>2</sub> (20 % weight ×  
 206 vol<sup>-1</sup>). All samples were stored at +4 °C until analysis in the home lab.

**207 2.2. Methane and carbon dioxide concentrations**

208 Prior to measurement, we introduced 3 mL of ultrapure helium gas as headspace while  
209 withdrawing the same amount of NaCl solution from the crimped vial. To equilibrate  
210 dissolved gases with the headspace, the content of the vials was mixed at 220 rpm on an  
211 orbital shaker for 18 h, and further vortexed to break up the remaining small clayey  
212 aggregates. A 250  $\mu\text{L}$  sample of the headspace gas was then extracted and introduced into a  
213 7890A Gas Chromatography System, which was equipped with both a flame ionization  
214 detector (FID) and a thermal conductivity detector (TCD), along with an HP PLOT Q column  
215 (all from Agilent). The oven temperature was set to 50  $^{\circ}\text{C}$ , the flow rate was maintained at  
216 17.2  $\text{mL min}^{-1}$ , and the pressure was held at 13 psi. Both detectors operated at 200  $^{\circ}\text{C}$  with  
217 flow rates of 40  $\text{mL min}^{-1}$  (FID) and 15  $\text{mL min}^{-1}$  (TCD). Calibration of the system was  
218 performed by injecting pure analytical standards with  $\text{CO}_2$  concentrations of 310 ppm and  
219 5270 ppm, as well as  $\text{CH}_4$  concentrations of 10 ppm and 5170 ppm. The initial  $\text{CH}_4$  and  $\text{CO}_2$   
220 concentrations were converted from ppm to molar concentrations using the ideal gas law.

**221 2.3. Cell counting**

222 Total cell counts were conducted following a protocol based on Kallmeyer et al. (2008).  
223 Sediment samples were initially diluted at a ratio of 1:100 using a 25  $\text{g L}^{-1}$  NaCl solution. 25  
224  $\mu\text{L}$  of the resulting slurry were uniformly distributed onto black 0.2  $\mu\text{m}$  polycarbonate  
225 Cyclopore membrane filters (Whatman International Ltd, Maidstone, UK) via vacuum  
226 filtration. For cell visualization, filters were stained with a mixture consisting of SYBR Green I  
227 (10  $\mu\text{L}$ ; Molecular Probes, Eugene, USA), phenylenediamine (100  $\mu\text{L}$ ), glycerol (300  $\mu\text{L}$ ), Milli-  
228 Q water (300  $\mu\text{L}$ ), and 300  $\mu\text{L}$  of VECTASHIELD<sup>®</sup> Antifade Mounting Medium (H-1000-10,  
229 Vector Laboratories, Burlingame, USA). A volume of 15  $\mu\text{L}$  of this staining solution was  
230 applied to each filter. The counting was performed using an epifluorescence microscope  
231 (Leica DM2000, Wetzlar, Germany) by counting cells in 200 fields of view. Cell abundances  
232 were calculated as  $\log_{10}$  cells per  $\text{cm}^3$  of sediment, based on triplicate measurements, with  
233 standard deviations consistently remaining below 15%.

**234 2.4. Pore water geochemistry**

235 Dissolved sulfate was quantified via suppressed Ion Chromatography (column: SykroGel A ×  
236 300 AB-A01; eluent: 7.3 mg L<sup>-1</sup> NaSCN and 636 mg L<sup>-1</sup> NaCO<sub>3</sub>; pump rate 1 mL min<sup>-1</sup>;  
237 injection volume 50 µL). The detection limit was 5 µM. Samples were measured in triplicate,  
238 with average relative standard deviations consistently below 3%.

239 Cation and trace elemental concentrations in the pore water were determined using high-  
240 resolution inductively coupled plasma mass spectrometry (HR-ICP-MS, ELEMENT 2XR,  
241 Thermo Scientific, Waltham, USA) at the EIMiE-labs at GFZ after acidifying the samples with  
242 ultrapure HNO<sub>3</sub>. Until analysis, the samples were kept anoxic to prevent precipitation and  
243 potential alteration of the metal concentrations. 100 µL of pore water was doped with 10 µL  
244 of an indium (In) standard solution at a concentration of 100 µg L<sup>-1</sup> and the samples were  
245 diluted with 2 vol% ultrapure HNO<sub>3</sub>. Trace elements were quantified by external calibration  
246 using single-element standards, carefully matched to the sample matrix. The acid blank was  
247 subtracted from each measurement. The detection limits for the applied ICP-MS routine  
248 typically ranged between 0.5 and 1 ng g<sup>-1</sup>, for the analytes. Measurement uncertainty,  
249 referring to the repeatability of the measurements, was about 2-5 % for all analyses.

250 Iron concentrations were analyzed separately using spectrophotometry, following the  
251 protocol described by Viollier et al. (2000). The detection limit of this method is 0.25 µM  
252 and the measurement uncertainty was approximately 5 % for all analyses. Sulfide was  
253 determined photometrically according to Cline (1969). The detection limit is 0.1 µM. All  
254 samples were measured in triplicates and the results were averaged with a standard  
255 deviation ≤ 3.5 %. Alkalinity was determined via titration using the Visocolor HE alkalinity AL  
256 7 kit (Macherey-Nagel GmbH) adapted to the sample volume of 500 µL. The detection limit  
257 is 0.15 mM and triplicate measurements differed by less than 3 %.

## 258 **2.5. Sediment inorganic fraction**

259 For XRF analysis, approximately 30 g of sediment material was freeze-dried, ground in agate  
260 mortars using a Fritsch Pulverisette 5 planetary mill at 300 rpm for 5 minutes, sieved  
261 through a 63 µm stainless steel mesh, and then melted with two Fluxana reference  
262 materials to form glass discs. These discs were analyzed using an AXIOS X-ray fluorescence  
263 (XRF) advanced spectrometer (Malvern Panalytical, United Kingdom), equipped with an End-

264 window RH X-ray tube SST-mAX at a 4 kW output. Elemental proportions were determined  
265 for major elements as oxides in weight % [wt %] (i.e. SiO<sub>2</sub>, Al<sub>2</sub>O<sub>3</sub>, Fe<sub>2</sub>O<sub>3</sub>, MnO, MgO, CaO,  
266 Na<sub>2</sub>O, K<sub>2</sub>O, P<sub>2</sub>O<sub>5</sub>, TiO<sub>2</sub>, SO<sub>3</sub>, loss on ignition (LOI)), and trace elements [ppm] (i.e. Ba, Cr, Zn,  
267 Ga, Nb, Ni, Rb, Sr, V, Y, Zr). Quantification limits for major elements were 0.02 wt % and  
268 approximately 10 ppm for trace elements. LOI was determined based on the mass  
269 difference before and after fusion. Reproducibility was evaluated using reference materials  
270 and better than 2% for all major elements.

## 271 **2.6. Statistical and geostatistical analyses**

272 Min-max normalization was applied to the XRF dataset, scaling all variables to a range  
273 between 0 and 1. PCA was then performed using the `prcomp()` function in R with centering  
274 and scaling enabled to identify patterns and relationships among chemical species in the  
275 solid sediment phase, reducing the data's dimensionality and highlighting key variability  
276 across samples. This analysis provided further insight into the underlying structure of the  
277 data, complementing the subsequent visualizations. For ternary visualization, selected  
278 standardized parameters were then proportionally scaled to sum to 100 %. In some cases,  
279 the resulting values of multiple compounds (e.g., those associated with specific mineral  
280 groups like carbonates) were summed. Thus, the ternary diagrams reflect only relative  
281 patterns and should not be interpreted in terms of absolute abundances.

282 We applied Mann–Whitney U tests (Mann and Whitney, 1947) using the function  
283 `wilcox.test()` to XRF and pore water data to assess whether the median values of individual  
284 chemical species differed significantly between groups. This non-parametric test was used  
285 to evaluate differences in concentration gradients in the pore water and absolute  
286 concentrations in the solid sediment phase between HC-affected zones (Z01, Z10, Z12) and  
287 reference sites (Ref5, Ref6), as well as among and within individual zones and sediment  
288 cores. To assess differences in variability (i.e. variance), we also used the Brown-Forsythe  
289 test (Brown and Forsythe, 1974) applying the `leveneTest()` function . This test allowed us to  
290 assess whether the variance in chemical species concentrations - reflecting chemical  
291 heterogeneity - varied significantly between zones. Finally, Pearson correlation analyses  
292 (Pearson, 1895; Sedgwick, 2012) were conducted on the pore water data to explore linear  
293 relationships among chemical species. Two analytical levels were considered: (1)

294 correlations within individual sediment cores, and (2) correlations across all cores from the  
295 same sampling zone (e.g., all cores from Z01). All statistical and geostatistical analyses were  
296 performed using R version 4.2.0 (R Core Team, 2022).

297 Diffusive fluxes of sulfate, alkalinity, and calcium across the sediment–water interface were  
298 calculated based on Fick's first law of diffusion using the linear concentration gradients.

299 Molecular diffusion coefficients were taken from Schulz (2006) and subsequently adjusted  
300 for sediment conditions following Iversen and Jørgensen (1993). To visualize spatial patterns

301 in fluxes of sulfate, alkalinity, and calcium, we applied ordinary kriging using the gstat

302 package in R (Pebesma, 2004). First, empirical variograms were calculated from spatially

303 referenced flux measurements. Several theoretical variogram models (spherical,

304 exponential, Gaussian, and Matérn) were fitted and compared. The best-fitting model was

305 selected based on convergence criteria and plausibility of the sill and range parameters. This

306 model was then used to interpolate flux values across a regular spatial grid covering the

307 study area. The resulting kriging maps (Matheron, 1963) provided continuous spatial

308 representations of flux gradients and enabled the identification of heterogeneities between

309 hydrocarbon seep zones and reference sites. Visualizations were created using the ggplot2

310 package (Wickham, 2016).

## 311 **2.7. Sediment organic fraction**

312 Molecular-level insights into the organic geochemistry of sediments were obtained for

313 solvent-extractable OM using Fourier Transform Ion Cyclotron Resonance Mass

314 Spectrometry (FT-ICR-MS). Based on geochemical pore water profiles, a subset of 11

315 representative samples consisting of three samples from each of the three HC zones (Z01,

316 Z10, Z12) and one sample from each of the two reference zones (Ref5, Ref6) was selected

317 from the total of 50 sediment cores. For each sample, approximately 10 g of sediment were

318 freeze-dried, milled, and the organic content was extracted using a Soxhlet extractor

319 following a procedure described by Poetz et al. (2014). The extraction was performed with a

320 solvent mixture composed of dichloromethane and methanol (v/v = 99:1) at 40 °C for 24

321 hours. The extracts were then analyzed at ultra-high mass resolution using a Bruker Daltonik

322 Solarix 12T FT-ICR-MS. Ionization was carried out using an Apollo II ESI source and an APPI-II

323 source (all from Bruker Daltonik GmbH, Bremen, Germany).

324 For electrospray ionization (ESI<sup>-</sup>), nitrogen was used as the nebulizing gas at a flow rate of  
325 4 L min<sup>-1</sup> at 220 °C and a pressure of 1.4 bar. The capillary voltage was set to 3000 V, and the  
326 collision-induced dissociation (CID) voltage was 60 V. The samples were infused at a flow  
327 rate of 2.5 µL min<sup>-1</sup> using a Hamilton syringe pump. The spectra were recorded in  
328 broadband mode using 8-megaword data sets. The ion accumulation time was 0.05 s, and a  
329 total of 200 scans were collected into the mass spectrum, covering a mass-to-charge ratio  
330 (m/z) range of 150–1000. For atmospheric pressure photoionization (APPI<sup>+</sup>), nitrogen was  
331 used as the nebulizing gas at a flow rate of 3 L min<sup>-1</sup> at 210 °C and a pressure of 12.3 bar.  
332 The capillary voltage was set to - 1000 V, and the CID voltage was 30 V. The samples were  
333 infused at a flow rate of 20 µL min<sup>-1</sup> using a Hamilton syringe pump. The spectra were  
334 recorded in broadband mode using 8-megaword data sets. The ion accumulation time was  
335 0.05 s, and a total of 300 scans were collected into the mass spectrum, covering an m/z  
336 range of 147–1500.

337 The resulting spectra were internally recalibrated (quadratic) with a standard deviation  
338 error of < 0.02 ppm, and only m/z values with a signal-to-noise ratio > 9 were exported for  
339 formula assignment. Formula assignment was performed using a combination of Bruker  
340 Analysis and Microsoft Excel, considering the isotopes <sup>12</sup>C and <sup>13</sup>C and the elemental ranges  
341 C<sub>x</sub>H<sub>y</sub>N<sub>0–2</sub>O<sub>0–10</sub>S<sub>0–2</sub>Na<sub>0–1</sub>. The mass tolerance was set to 5 ppm.

### 342 **3. Results**

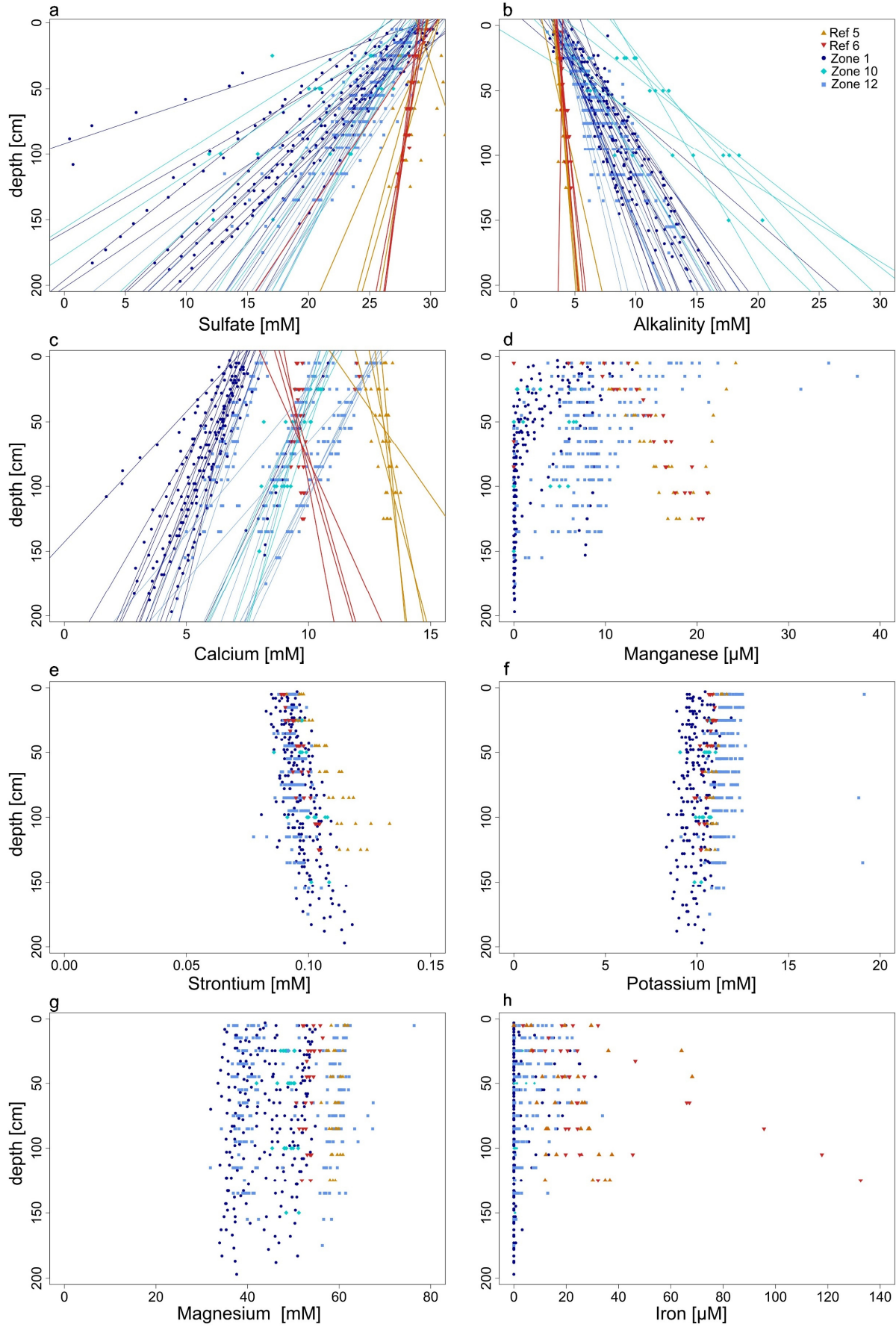
#### 343 **3.1. Methane and carbon dioxide concentrations and cell abundances**

344 All samples contain measurable methane concentrations, ranging from 0.08 to 19.79 µM.  
345 While samples from reference sites contain less than 5 µM of methane, higher  
346 concentrations are restricted to few samples from HC-affected sites, all located deeper than  
347 100 cm below seafloor (cmbsf). CO<sub>2</sub> was detectable in all samples, with concentrations  
348 ranging from 29 µM to 512 µM, without any site-specific trend (Supplementary Fig. S1). This  
349 is likely due to carbonate buffering, with dissolved CO<sub>2</sub> equilibrating with bicarbonate and  
350 carbonate in pore water at both HC-affected and reference sites. In both cases, low gas  
351 concentrations prevented measurement of their stable isotopic signatures.

## Imprint of minute hydrocarbon seepage on sedimentary fractions

352 Total cell counts are approximately  $10^7$  cells  $\times$  cm<sup>3</sup> across all sediment cores, with no  
353 significant variation with depth (Supplementary Fig. S2). The mean deviation of cell counts  
354 within samples is around 12%.

# Imprint of minute hydrocarbon seepage on sedimentary fractions



355

356

**Figure 2: Pore-water profiles for some representative parameters.** The profiles for sulfate concentrations (a),

357 alkalinity (b), and calcium (c) show both data points and regression lines ( $R^2 > 0.8$ ). The regression lines for HC-  
 358 affected zones (Zone 1, Zone 10, Zone 12) show steeper gradients compared to those from reference zones  
 359 (Ref 5, Ref 6). The profiles for magnesium (d), strontium (e), potassium (f), magnesium (g), and iron (h) are  
 360 shown as data points due to the insufficient  $R^2$  value of their respective regression lines.

### 361 **3.1. Pore water profiles**

362 Both sulfate and alkalinity concentrations exhibit strong linear decreasing and increasing  
 363 trends ( $R^2 \geq 0.85$ ) with depth (Figs. 2a and 2b), respectively. The gradients are steeper in the  
 364 HC-affected zones compared to reference zones. Based on linear extrapolation, sulfate  
 365 depletion would be reached at ca. 3 and 12 mbsf in HC and reference zones, respectively.  
 366 Sulfide concentrations are below the detection limit ( $1 \mu\text{M}$ ) in all cores from reference zones  
 367 and in most of the cores from Z12 (only 2 out of 17 cores have detectable sulfide;  
 368 Supplementary Fig. S3). In contrast, in most cores from Z01 (12 out of 15) and Z10 (4 out of  
 369 7), sulfide concentrations increase with depth.

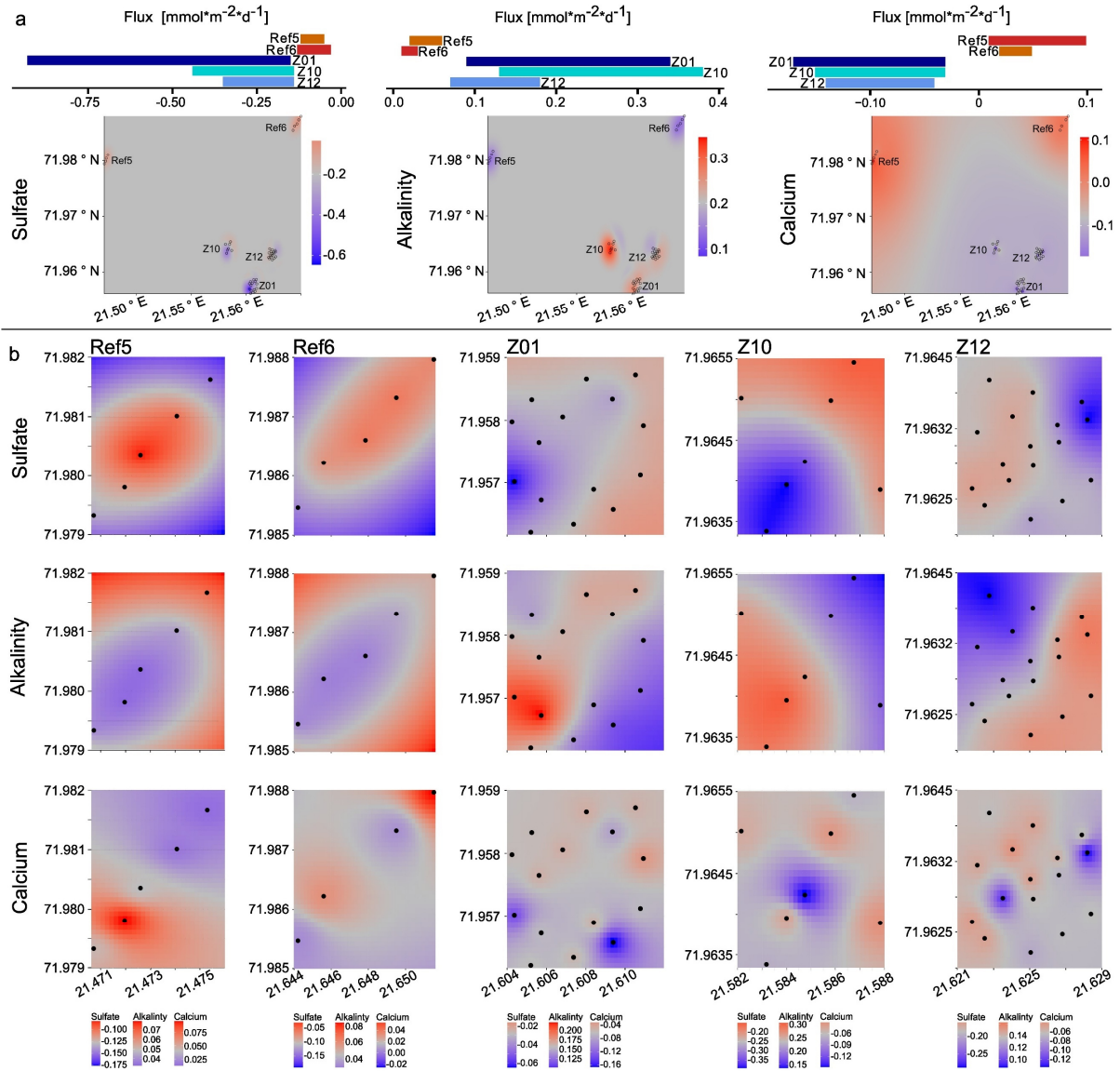
370 In the reference zones concentrations of pore water  $\text{Ca}^{2+}$  increase with depth (Fig. 2c,  
 371 Supplementary Fig. S3), but decrease in the HC-affected zones. For  $\text{Mn}^{2+}$  concentrations also  
 372 increase with depth in the reference zones (Fig. 2d, Supplementary Fig. S4). In most of the  
 373 cores from HC-affected zones,  $\text{Mn}^{2+}$  pore water profiles show a decreasing trend with  
 374 depth, but with distinct patterns, of which each one is predominant in a different sampling  
 375 zone: (1) in Z01 many profiles show concentrations decreasing from ca.  $15 \mu\text{M}$  at the SWI to  
 376 near zero at ca. 75 cmbsf; (2) in Z12 concentrations decrease from ca.  $15 \mu\text{M}$  at the SWI but  
 377 then stabilize around  $5 \mu\text{M}$  at 1 mbsf; (3) in Z10 and Z12 some concentrations profiles  
 378 remain constant around  $7 \text{ mM}$  throughout depth.

379 Pore water concentrations for  $\text{Cu}^{2+}$ ,  $\text{Si}^{4+}$ ,  $\text{Zn}^{2+}$ ,  $\text{Mg}^{2+}$  and  $\text{K}^+$  remain almost unchanged in with  
 380 depth in both HC-affected and reference zones (Figs. 2e-2g, Supplementary Figs. S4-S5),  
 381 whereas  $\text{Sr}^{2+}$  concentrations increase in cores from both HC-affected zones and reference  
 382 zones, but more pronounced for the latter (Fig. 2e). Dissolved  $\text{Fe}^{2+}$  is rarely detectable in  
 383 cores from the HC-affected zones and falls below detection limit within the upper 1 mbsf  
 384 (Fig. 2h). In most cores from reference zones, pore water  $\text{Fe}^{2+}$  is detectable and  
 385 concentrations increase with depth.  $\text{Ba}^{2+}$  was measurable only in few cores from Z01, with

386 concentrations increasing with depth (Supplementary Fig S4). With few exceptions,  $\text{Ni}^{2+}$  and  
 387  $\text{As}^{2+}$  remain below the detection limit in all samples at all depths.

388 **3.2. Statistical analyses of inter- and intrazonal variations**

389 **3.2.1. Comparative analysis of pore water geochemistry**



390  
 391 **Figure 3. Spatial variability and flux patterns of sulfate, alkalinity, and calcium across different zones.** (a) Bar  
 392 plots show the mean areal fluxes (mmol m<sup>-2</sup> d<sup>-1</sup>) of sulfate (left), alkalinity (middle), and calcium (right) at the  
 393 five zones (Ref5, Ref6, Z01, Z10, Z12). Kriging-interpolated maps illustrate the spatial distribution of these  
 394 fluxes across the study area. Color gradients indicate the direction and magnitude of fluxes. (b) Detailed kriging  
 395 maps of sulfate (top row), alkalinity (middle row), and calcium (bottom row) fluxes at each zone. Each column  
 396 corresponds to one zone, showing localized spatial variability in solute fluxes. Black dots indicate the sampling  
 397 sites.

398 The Mann-Whitney U tests (Mann and Whitney, 1947) confirmed statistical significance for  
399 steeper sulfate and alkalinity gradients (Fig. 2, Supplementary Table S2) in HC-affected  
400 zones ( $p_{\text{SO}_4} = 3.86\text{E-}10$ ,  $p_{\text{alk}} = 2.74\text{E-}05$ ); opposite trends in  $\text{Ca}^{2+}$  profiles ( $p_{\text{Ca}} = 1.40\text{E-}04$ ); and  
401 different pore water gradients in  $\text{Mn}^{2+}$  concentrations ( $p_{\text{Mn}} = 5.38\text{E-}06$ ), assuming linear  
402 profiles which in some cases did not provide the best fit (Fig. 2, Supplementary Fig. S4 and  
403 porewater profile descriptions in Section 3.1). The results for manganese should therefore  
404 be considered as approximations.

405 The Brown-Forsythe tests (Brown and Forsythe, 1974) further confirmed that the variance  
406 for pore water  $\text{SO}_4^{2-}$ , alkalinity,  $\text{Ca}^{2+}$ , and  $\text{Mn}^{2+}$  gradients is smaller within reference zones  
407 (all p-values < 0.05, Supplementary Table S3) than within HC-affected zones (Fig. 2). In  
408 addition, a comparison of the variances across individual HC zones and reference zones  
409 indicates significant differences in most instances.

410 Kriging plots for sulfate, alkalinity and calcium fluxes (which are proportional to their  
411 gradients) enabled the visualization of spatial variations over the entire study area and  
412 within the sampling zones (Fig. 3). The resulting patterns of variability align with previous  
413 statistical tests and highlight the different spatial heterogeneity between reference and HC-  
414 affected areas, with notably a stronger variability among those exposed to seepage.

### 415 *3.2.2. Pore water species within and across cores*

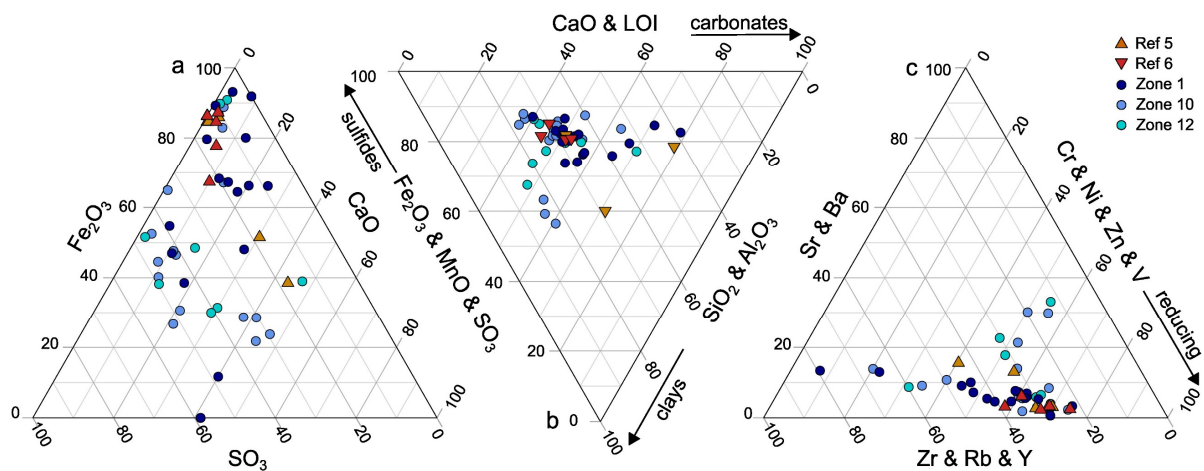
416 We also performed intra- and intervariation analyses, i.e. we investigated the correlation of  
417 chemical species within each core using Pearson Correlation (Pearson, 1895; Sedgwick,  
418 2012). We found a strong correlation (average  $|r| > 0.86$ ) between sulfate, alkalinity and  
419 calcium and, to a lesser extent (average  $|r| > 0.66$ ) with manganese in almost every  
420 individual core from HC zones. In contrast, within reference zones, we only found  
421 correlations between alkalinity and sulfate (average  $r > -0.76$ ) as well as alkalinity and  
422 manganese (average  $r > 0.86$ ) (Supplementary Table S4).

423 To determine whether concomitant biogeochemical processes may occur in different cores,  
424 we assessed the correlation between pore water gradients for each of the 5 sampling zones  
425 separately, resulting in 10 combinations of alkalinity, sulfate, manganese, calcium, and  
426 sulfide. For cores from reference zones, a negative correlation between sulfate and

427 alkalinity was observed ( $r = -0.80$  and  $-0.85$  for Ref5 and Ref6). In addition, for Ref5,  
 428 additional correlations were found between sulfate and manganese ( $r = -0.99$ ), alkalinity  
 429 and calcium ( $r = -0.86$ ) and alkalinity and manganese ( $r = 0.78$ ). For cores from the three HC  
 430 HC zones, no significant correlations ( $r < 0.7$ ) were found between geochemical species,  
 431 except at Z10 between sulfate and alkalinity ( $r = -0.89$ ), alkalinity and sulfide ( $r = 0.77$ )  
 432 (Supplementary Table S4).

433 *3.2.3. XRF elemental concentrations of the sediment inorganic fraction*

434 CaO and SO<sub>3</sub> concentrations are significantly higher (Mann-Whitney U test,  $p < 0.05$ ) in  
 435 sediments from HC-affected than reference zones. Despite similar behavior as alkaline-earth  
 436 elements, Ba ( $p = 0.11$ ) and Sr ( $p = 0.17$ ) were only slightly more abundant in sediments  
 437 exposed to seepage. Conversely, the relative abundance of Fe<sub>2</sub>O<sub>3</sub>, P<sub>2</sub>O<sub>5</sub>, Ti, Cr, and Zn is  
 438 higher ( $p < 0.05$ ) in cores from reference zones, while Al ( $p = 0.06$ ), Ni ( $p = 0.05$ ), Mn ( $p =$   
 439  $0.12$ ), and V ( $p = 0.05$ ) show a tendency towards higher relative abundances. The loss on  
 440 ignition (LOI) is significantly higher ( $p < 0.05$ ) in cores from reference zones.



441  
 442 **Figure 4. Ternary diagrams showing the relative proportions of selected major and trace elements in solid**  
 443 **phase sediments from hydrocarbon HC zones and reference zones. (a) Major elements: Fe<sub>2</sub>O<sub>3</sub>–SO<sub>3</sub>–CaO, (b)**  
 444 **major elements grouped by associated mineral fractions: CaO and LOI (carbonate), Fe<sub>2</sub>O<sub>3</sub> and MnO and SO<sub>3</sub>**  
 445 **(sulfide), and SiO<sub>2</sub> and Al<sub>2</sub>O<sub>3</sub> (clay), and (c) trace elements grouped by geochemical behavior: Cr, Ni, Zn and V**  
 446 **(redox-sensitive), Sr and Ba (calcite-, barite-associated), and Zr, Rb and Y (conservative). Each symbol**  
 447 **represents an individual sample. HC zones (blue colors) and reference zones (red colors) largely overlap, the**  
 448 **scatter in the HC zones is noticeably larger, indicating a greater variance.**

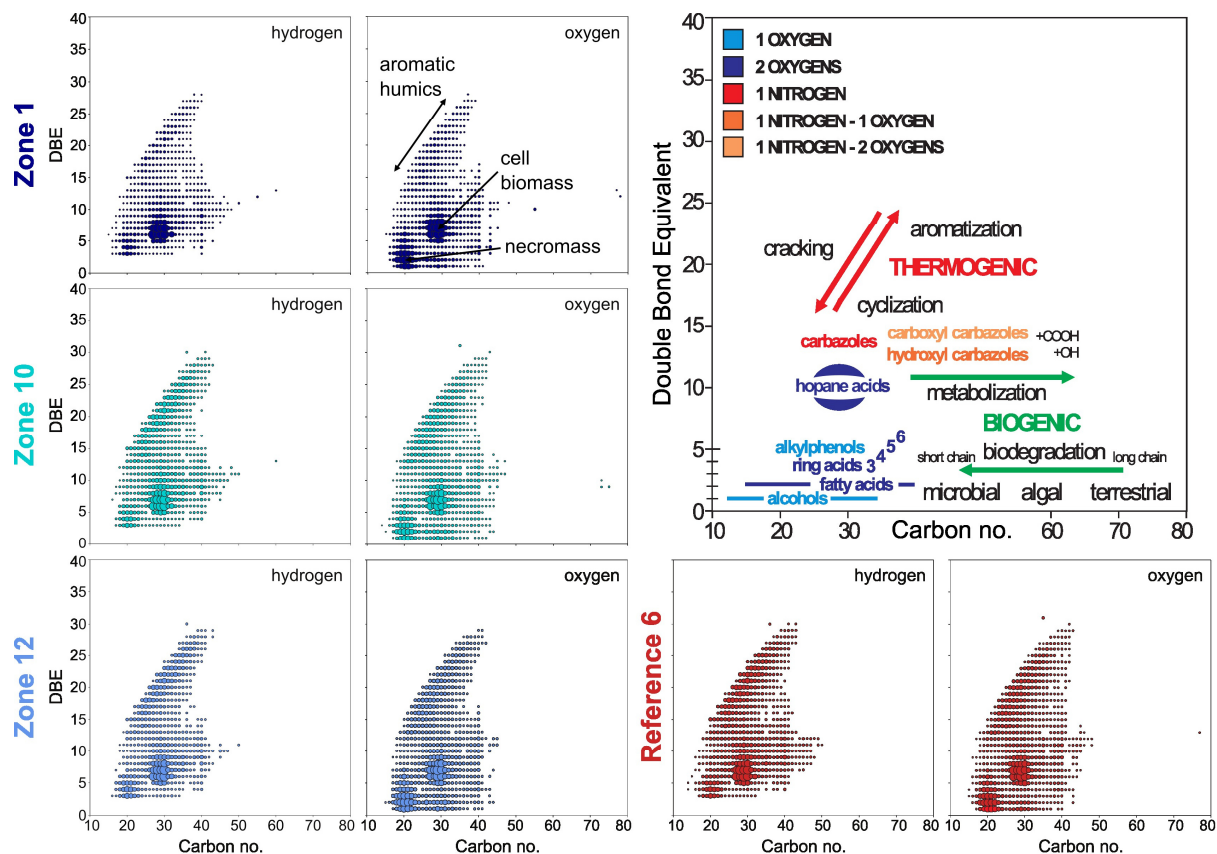
449 Significant differences ( $p < 0.05$ ) revealed by the Brown-Forsythe variance homogeneity test  
450 included Ba and  $\text{SO}_3$  concentrations at seepage and reference zones, highlighting higher  
451 variance among cores from HC-affected zones. Variance in CaO concentrations appeared  
452 non-significant ( $p = 0.09$ ). Major and trace element in ternary diagrams (Fig. 4) confirm this,  
453 as the variance (scatter) is noticeably greater in the HC zones compared to the reference  
454 zones. Despite considerable overlap, this observation is consistent with the results of the  
455 Brown-Forsythe test, illustrating the lower variance across samples from reference zones  
456 compared to HC zones. This pattern is further supported by PCA of major and trace  
457 elements (Supplementary Figs. S6–S7), where samples from HC zones show greater  
458 dispersion along the first principal component (60.7% and 59.8% variance explained,  
459 respectively), indicating higher variability in both major and trace element composition.

### 460 **3.3. Organic compound classes across sampling zones**

461 The number of mass spectrometry signals and their distribution across different compound  
462 classes (e.g., pure HCs, HCs with O, N, and S atoms), measured in both ionization modes  
463 (APPI+ and ESI-) and analyzed in various data representations, appear very similar for both  
464 seepage and reference sites. Atomic H/C and O/C ratios derived from assigned molecular  
465 formulas showed no significant differences between seep and reference sites. Additionally,  
466 the degree of unsaturation (i.e. double bond equivalent, DBE) relative to the number of  
467 carbon atoms does not show significant variations in the relative abundance of different  
468 compound classes or noticeable differences across sampling sites (Fig. 5, Supplementary Fig.  
469 8).

470 Specific molecular signatures indicative of microbial biomass (e.g. hopanoids) and degraded  
471 OM (e.g. humic acids) are also comparable across sampling zones (Fig. 5). Similar to total cell  
472 counts, molecular clusters assigned to hopanoid-derived compounds (typically around 6–8  
473 DBE and ~30 carbons) occur in similar abundance at all sites, suggesting comparable  
474 microbial population sizes. Likewise, signals corresponding to fatty acids (low DBE, low  
475 number of carbons), which can be interpreted as cell remnants or necromass, are evenly  
476 distributed. Finally, aromatic compounds which are typically associated with humic  
477 substances from highly degraded and refractory OM, are equally present in sediments from  
478 all sampling zones. Signatures of seepage-related hydrocarbons, including saturated alkanes

479 and polyaromatic hydrocarbons typically associated with migrated oil and gas, were not  
 480 detected.



481  
 482 **Figure 5. Diagrams for molecular polar compounds identified by FT-ICR-MS in APPI+ mode in sediment**  
 483 **extracts from the three hydrocarbon HC zones and one reference zone. (From left to right) Double bond**  
 484 **equivalents (DBE) plotted against carbon number for compounds containing hydrogen and oxygen, and**  
 485 **simplified interpretative framework of some molecular classes (e.g. aromatic acids, hopane acids,**  
 486 **alkylphenols) and the expected shifts related to biogenic (e.g. microbial degradation) vs. thermogenic (e.g.**  
 487 **cracking, aromatization) processes.**

488 **4. Discussion**

489 In the SW Barents Sea, sediments are particularly organic-lean, with TOC values below 0.5 %  
 490 (Knies and Martinez, 2009). This low organic content enables the detection of discrete HC  
 491 seeps, as even a slight supply of electron donors can result in a direct increase in the  
 492 metabolic activity of HC-degrading microbial populations (Joye, 2020). This increase in  
 493 metabolic activity, along with the resulting geochemical redox changes, can be distinguished  
 494 from the background signal corresponding to pristine conditions at the seabed. In  
 495 comparison, any microbial or geochemical signal arising from inconspicuous HC seepage in

496 organic-rich environments would be obscured by ongoing OM breakdown, hampering  
497 discrimination of specific microbial populations or metabolic pathways involved in the  
498 degradation of discrete HCs.

#### 499 **4.1. Organic signatures of potentially active seepage remain elusive**

500 At seepage sites, we expected a greater diversity and higher concentrations of oxygen-  
501 containing compounds in the FT-ICR-MS mass spectra due to the formation of aromatic-ring  
502 radicals and by-products (e.g. alcohols, organic acids) during microbial HC degradation  
503 (Radovic and Silva, 2025). In sediments not exposed to seepage, these compounds should  
504 be less abundant, with overall a lower proportion of oxygenated components. However,  
505 because seepage and reference sites showed similar compound class distributions (Fig. 5;  
506 Supplementary Fig. S8), our data suggest that HCs had already been degraded at sediment  
507 depths below the reach of our cores, or converted into compounds with chain lengths that  
508 are too short for FT-ICR-MS detection. Instead, the FT-ICR-MS analysis only captured the  
509 background signal of the subseafloor sediments (i.e. biomass, necromass, organic residues),  
510 the corresponding compound class concentrations being consistent with similar microbial  
511 cell counts across seepage and reference sites (Supplementary Fig. 2). Thus, the suitability of  
512 this classical oil (and gas) analytical tool (Marshall and Rodgers, 2004) appears to be limited  
513 in the context of inconspicuous seepage, indirectly supporting our basic assumption of  
514 inconspicuous HC seepage in the HC-affected zones, without any indication for increased  
515 microbial biomass at seep sites.

#### 516 **4.2. Hydrocarbon seepage shapes redox zonation with precipitation of carbonate and** 517 **sulfide minerals**

518 Marine sediments exhibit a clear redox zonation, ranging from the aerobic respiration zone  
519 near the surface, transiting through the nitrate,  $Mn^{4+}$  and  $Fe^{3+}$  reduction zones to the sulfate  
520 reduction zone and methanogenesis (Froelich et al., 1979; Jørgensen and Kasten, 2006). In  
521 the sulfate reduction zone, sulfate acts as the electron acceptor leading to the production of  
522 hydrogen sulfide, bicarbonate, and water. The increase of these compounds in the pore  
523 water promotes precipitation of carbonates (e.g. calcite) and sulfide minerals (e.g., pyrite)  
524 (Smrzka et al., 2020; Smrzka et al., 2024; Lin et al., 2016; Peckmann et al., 2001).

525 Consequently, the incorporation of calcium, magnesium, strontium, iron, manganese, and  
526 trace elements (e.g., Cu, Ni, Zn) into these minerals leads to their depletion in pore water  
527 and enrichment in the sediment's inorganic fraction (Smrzka et al., 2019; Schippers and  
528 Jørgensen, 2001).

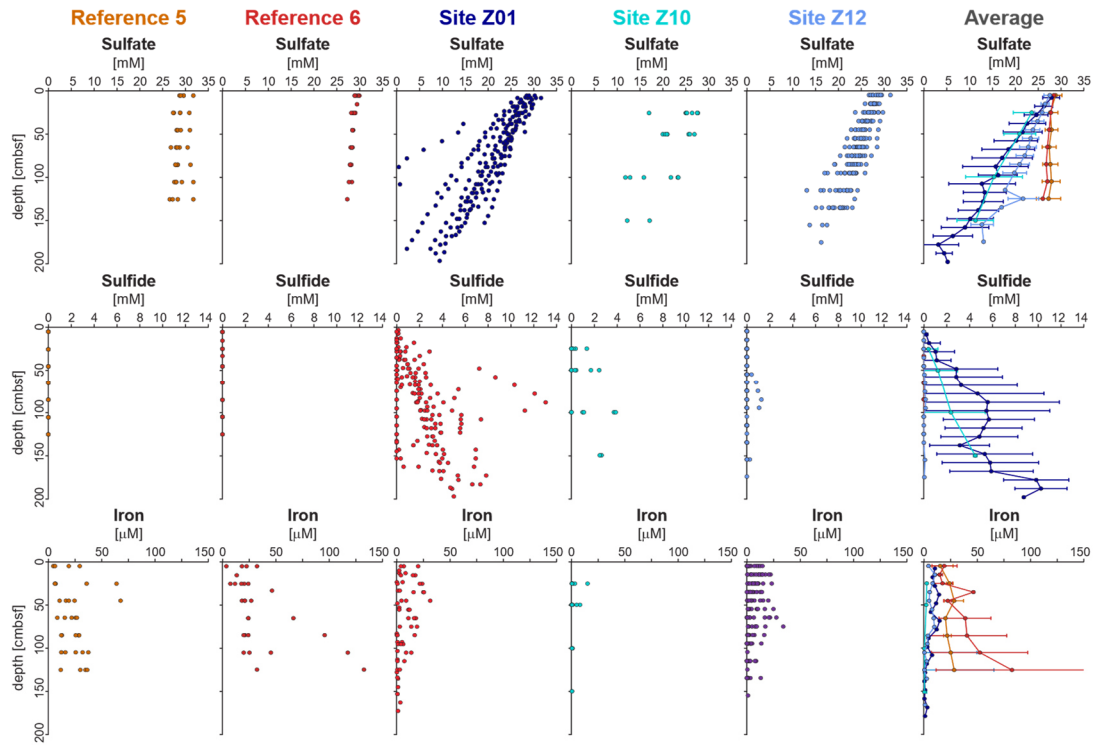
529 Both sediment geochemistry (Fig. 4, Supplementary Figs. S6-S7) and pore water analyses  
530 (Fig. 2, Supplementary Figs. S3-S5) confirmed the presence of diagenetic carbonates in  
531 sediments from HC zones. On the one hand, CaO, MgO, and Sr abundances increased in the  
532 solid phase. On the other hand, pore water  $\text{Ca}^{2+}$  concentrations decreased while alkalinity  
533 simultaneously increased with depth (Fig. 2). In contrast,  $\text{Mg}^{2+}$  and  $\text{Sr}^{2+}$  concentrations in  
534 pore water remained largely unchanged. Notably, incorporation of  $\text{Mg}^{2+}$  and  $\text{Sr}^{2+}$  into  
535 carbonate minerals is kinetically restricted compared to  $\text{Ca}^{2+}$  (Knight et al., 2023; Alkhatib et  
536 al., 2022) and, as carbonate precipitation could occur over relatively short time periods (i.e.  
537 during active seepage), substitution by pore water  $\text{Mg}^{2+}$  and  $\text{Sr}^{2+}$  appeared incomplete, thus  
538 their concentrations remained almost unchanged. Although methane-derived carbonates  
539 are typically high-Mg calcites or aragonite, we infer that the diagenetic carbonates in our  
540 study are likely low-Mg calcites. Alternatively, the recrystallization of metastable carbonate  
541 phases (e.g. aragonite) would release  $\text{Sr}^{2+}$  into the pore water (Hoareau et al., 2010). In  
542 contrast to the HC zones, pore water alkalinity,  $\text{Ca}^{2+}$  and  $\text{Sr}^{2+}$  concentrations increase with  
543 depth at the reference sites, while CaO and Sr contents remain low in the solid phase (Fig. 2,  
544 Supplementary Fig. S3). These trends indicate that precipitation and dissolution of  
545 carbonate minerals occurred (Schneider et al., 2006; Bach, 2024; Hoareau et al., 2010;  
546 Smrzka et al., 2019) under seepage and non-seepage conditions, respectively.

547 Although barium ( $\text{Ba}^{2+}$ ) can theoretically substitute for  $\text{Ca}^{2+}$  in carbonate minerals, its larger  
548 ionic radius and strong affinity for sulfate typically limit its incorporation. Instead,  $\text{Ba}^{2+}$   
549 precipitates as barite ( $\text{BaSO}_4$ ), which tends to dissolve under sulfate-reducing conditions  
550 (Carter et al., 2020; Von Breyman et al., 1992). Indeed,  $\text{Ba}^{2+}$  was detectable in pore water  
551 in only a few cores from HC-affected Zone 1 (Supplementary Fig. S4), where concentrations  
552 increased with depth. This pattern suggests localized barite dissolution, likely triggered by  
553 reducing conditions and upward fluid flow. Consistently, solid-phase data show elevated  
554  $\text{Ba}^{2+}$  concentrations in HC-affected zones relative to reference sites (Fig. 4, Supplementary

555 Tables S2), indicating barite accumulation through biogeochemical processes linked to HC  
556 seepage. These observations highlight the dynamic interplay between sulfate availability,  
557 redox zonation, and mineral precipitation at seepage sites, promoting barite formation but  
558 also sulfide mineralization.

559 At seepage sites, linear profiles in pore water sulfide revealed upward diffusion  
560 (Supplementary Fig. S3) and, given the low sulfate reduction rates previously measured in  
561 the corresponding interval (Schnabel et al., 2025), this sulfide likely originates from deeper  
562 sediment layers. When reactive metals, such as  $\text{Fe}^{2+}$ ,  $\text{Mn}^{2+}$ , and other trace metals dissolved  
563 in pore water, meet with ascending sulfide, precipitation of metal sulfides occurs,  
564 contributing to an accumulation of redox sensitive metals and sulfur in the solid phase. This  
565 is in line with observations from e.g. seeps sites in Guaymas basin (Kars et al., 2025). At  
566 reference sites, dissolved sulfide is absent while  $\text{Fe}^{2+}$  and  $\text{Mn}^{2+}$  concentrations increase in  
567 the pore water (Fig. 6, Supplementary Fig. S3, Supplementary Fig. S4) , suggesting that  
568 anaerobic respiration of solid-phase Fe(III) and Mn(IV) oxides prevails over sulfate reduction  
569 and that precipitation of metal sulfides does not take place, at least not on a quantitatively  
570 significant level. Because higher pore water sulfide concentrations in our samples generally  
571 correlate with elevated sulfur (i.e.  $\text{SO}_3$ ) (Fig. 6) concentrations in the solid phase, sulfide  
572 precipitation and sulfur accumulation allow to distinguish seepage sites from reference  
573 sites, where they remain systematically low. This further demonstrates that local differences  
574 in sulfide production or flux rates, as well as metal availability, may result from seepage in  
575 the sediment.

## Imprint of minute hydrocarbon seepage on sedimentary fractions



576

577 **Figure 6. Porewater profiles of sulfate, sulfide, and dissolved iron across five sites, including site**  
 578 **averages. In seep-affected cores, iron concentrations decrease where sulfide increases, indicating**  
 579 **removal of reactive iron through sulfide precipitation. Sulfate generally decreases with depth across**  
 580 **all sites. Error bars represent site-specific averages where applicable.**

581 Besides major element dynamics, HC seepage also alters biogeochemical cycling of trace  
 582 metals through its influence on redox zonation and authigenic mineral formation, thereby  
 583 exerting control on their mobility or retention in the sediment column. Trace element  
 584 incorporation into sulfide minerals vary between oil- and methane-dominated seep  
 585 environments, with higher concentrations of elements like Mn, Mo, Cu, and Zn often  
 586 observed in oil seep pyrites (Smrzka et al., 2024). At both seepage and reference zones,  
 587 redox-sensitive trace metals (e.g. Zn, Ni, and V; Cr to a lesser extent) can be transported in  
 588 solution upward from deeper sediment layers and precipitate locally depending on sulfate  
 589 reduction and other redox-dependent activities. At seepage sites, methanotrophic sulfate  
 590 reduction and AOM-driven processes enhance neoformation of sulfides and carbonates  
 591 which act as sinks for trace metals at seep sites, in particular pyrite (Smrzka et al. (2019);  
 592 Smrzka et al. (2024); Miao et al. (2022)). In contrast, lower SR activity and lesser mineral  
 593 precipitation at reference sites allow trace elements to continuously diffuse upward and be  
 594 captured under suboxic conditions via adsorption or precipitation as iron (oxyhydr)oxides.  
 595 Altogether, despite similar concentrations in the pore fluid across sampling sites

596 (Supplementary Table S2), the degree and depth of occurrence of sulfate reduction govern  
597 whether dissolved metal ions are sequestered in specific geochemical zones or bypass the  
598 redox gradient. Nevertheless, trace metal concentrations may also vary with redox  
599 gradients, precipitation kinetics, and phase-specific affinities (Smrzka et al. (2019),  
600 hampering the use of pore water or solid phase concentration as a proxy for HC seepage.  
601 Hence, a combined assessment of pore water geochemistry, redox zonation, and authigenic  
602 minerals offers a more suitable approach for seepage characterization. Although our bulk  
603 sediment geochemical data do not specifically target sulfide mineral phases, these findings  
604 highlight the potential of geochemical signatures to record different seepage types.

#### 605 4.3. Pore water fluxes and diagenetic minerals reflect the dynamics of transient seepage

606 Linear profiles for pore water alkalinity,  $\text{SO}_4^{2-}$ , and  $\text{Ca}^{2+}$  suggest no net turnover within the  
607 sampled sediment interval (Schulz, 2006). This stands in contradiction with our observations  
608 of the solid-phase geochemistry, which is indicative of carbonate and sulfide mineral  
609 formation in HC-affected zones. We suggest that the sulfate-methane transition zone  
610 (SMTZ), where most sulfide and carbonate precipitation occur, may have undergone  
611 temporal and spatial depth fluctuations, driven by variations in HC flux over time. Such  
612 fluctuations are well-documented and influenced by multiple factors, including  
613 sedimentation rate, temperature, OM availability (Dale et al., 2008) and hydrostatic  
614 pressure, which in the Barents Sea is particularly shaped by glacial-interglacial dynamics  
615 (Argentino et al., 2021; Nickel, 2013).

616 In the Barents Sea, low sedimentation rates combined with extensive glacial history are  
617 inferred to have shaped SMTZ dynamics. During the Last Glacial Maximum (~20 ka),  
618 grounded ice sheets prevented seawater sulfate diffusion into the sediment in the Barents  
619 Sea (Andreassen et al., 2008; Siegert et al., 2001), shifting the SMTZ upward. Following  
620 deglaciation (~14 ka) (Elverhøi et al., 1993), seawater reoccupied the seafloor, restoring  
621 sulfate supply and initiating a progressive downward migration of the SMTZ. Processes such  
622 as gas hydrate dissociation and associated methane release during ice retreat (Nickel et al.,  
623 2013) further enhanced these dynamics. Comparable patterns have been observed  
624 elsewhere in the Barents Sea, where post-glacial rebound and HC flux variations have  
625 caused significant SMTZ fluctuations (Argentino et al., 2021).

626 The occurrence of diagenetic carbonates and sulfides resulting most probably from past  
627 AOM processes at the (paleo)SMTZ are therefore best understood as products of these  
628 historical boundary conditions. Their accumulation in the sediment, in combination with  
629 present-day linear pore water profiles, suggests that the system currently reflects a stage of  
630 subdued seepage activity, and consequently deeper SMTZ. Thus, the present-day mineral  
631 assemblage provides a cumulative archive of past seepage episodes rather than a snapshot  
632 of ongoing processes, highlighting a key limitation of interpreting solid-phase geochemistry  
633 alone. Although an increased presence of carbonates and sulfides may be indicative of past  
634 redox conditions and fluid flow, these minerals cannot reliably distinguish active from relict  
635 seepage. Integration with pore water profiles and other dynamic indicators remains  
636 essential to reconstruct seepage history and assess present-day activity.

637 Overall, our findings align with typical mineralogical signatures of weak HC seeps, commonly  
638 with carbonate (CaO) contents of 1-3 wt% (Rovere et al., 2020; Karaca et al., 2010) and  
639 sulfur (SO<sub>3</sub>) concentrations below 1 wt % (Fischer et al., 2012), thereby matching our  
640 seepage site values (i.e. 2.1 wt% CaO, 0.8 wt% SO<sub>3</sub>). The reference sites or our study exhibit  
641 values (i.e. 1.5 wt% CaO, 0.2 wt% SO<sub>3</sub>) that are consistent with background diagenesis  
642 typically observed in non-seep environments (1–2 wt% CaO, <0.2 wt% SO<sub>3</sub>) (Fischer et al.,  
643 2012; Karaca et al., 2010). Thus, we observe that carbonate and sulfide enrichments  
644 documented in Barents Sea sediments represent the imprint of past seepage episodes,  
645 whereas present-day pore water profiles reflect a current state of low, or absent, HC flux  
646 within the sampled interval.

#### 647 **4.4. Fine-scale heterogeneity characterizes weak hydrocarbon seepage**

648 The HC zones are affected by inconspicuous, diffuse seepage with very low sulfate flux rates  
649 below 1 mmol × m<sup>-2</sup> × d<sup>-1</sup> (Fig. 3). Typical fluxes at seeps range from 1–10 mol × m<sup>-2</sup> × d<sup>-1</sup> for  
650 high flux seeps, e.g. Coal Oil Point Seep Field, Santa Barbara, California (Padilla et al., 2019),  
651 and 0.1–1 mol × m<sup>-2</sup> × d<sup>-1</sup> for moderate flux seeps, e.g. North-western Black Sea (Hu et al.,  
652 2012). Since seepage-induced biogeochemical processes, like AOM and concomitant  
653 carbonate precipitation, predominantly occur below our sampling depth range (Schnabel et  
654 al., 2025), their effects can be detected only indirectly. For instance, the steeper sulfate  
655 gradients observed in the HC zones compared to the reference zones (Fig. 3, Supplementary

656 Fig. S3) suggest increased sulfate reduction rates due to HC supply from below. Geochemical  
657 fluxes at the seepage sites show considerable variability across individual cores (Fig. 3),  
658 which is considered a typical feature of seep environments inherent to localized differences  
659 in fluid flow, microbial activity, or redox conditions (Pop Ristova et al., 2015; Foster et al.,  
660 2015; Schnabel et al., 2025). In contrast, reference sites present rather uniform conditions,  
661 as they primarily reflect sedimentation, OM input and diffusion at the sediment-water  
662 interface rather than seepage.

663 In addition to variable fluxes reported for cores from seepage sites, the pattern of  
664 interconnected geochemical parameters also differs on a spatial scale (Supplementary Table  
665 S4). While a single pore water species may correlate in all 50 individual cores (e.g. sulfate  
666 concentrations and alkalinity), ratios between parameters appear to be different for each  
667 core across different HC-affected sites, and even within each individual seepage site  
668 sampled. This suggests that, even though similar microbial processes (e.g. denitrification  
669 reduction, sulfate reduction), can be expected to take place throughout the sampled area,  
670 their degree of intensity and interactions vary on a small spatial scale, leading to  
671 considerable local differences both within and between HC zones. In contrast, such  
672 correlations are much better both within and across cores from reference sites (Fig. 5),  
673 indicating more homogeneous and predictable diagenetic conditions.

## 674 **5. Conclusions**

675 This study elucidates the geochemical and mineralogical imprints of inconspicuous HC  
676 seepage on near-seafloor sediments in the southwestern Barents Sea. Extremely low  
677 element fluxes with often complete degradation of HCs in sediment layers below the  
678 sampling depth of this study posed significant challenges in the detection of active seepage.  
679 This explains why the FT-ICR-MS-based approach was unsuccessful in identifying diagnostic  
680 organic compounds, as volatile and short-chained organic compounds cannot be resolved.  
681 In contrast, inorganic geochemical signatures provided indirect evidence of seepage-related  
682 reductive diagenetic processes. Elevated pore water alkalinity alongside decreasing  $\text{Ca}^{2+}$   
683 concentrations with depth, substantiated by elemental enrichments in the solid phase were  
684 clear indications of carbonate precipitation. In addition, pore water depletion of sulfate and

685 manganese concomitant with increased solid phase sulfide concentrations point towards  
686 formation of sulfide minerals. In summary, many geochemical processes along strong seeps  
687 can also be directly or indirectly detected for minor HC seeps where the HCs are  
688 metabolized below the sampling interval.

689 Pronounced spatial variability in geochemical gradients across seepage-affected sites was  
690 observed, revealing local heterogeneity in fluid flow and redox conditions as a result of  
691 variable seepage intensity. Otherwise, correlated geochemical parameters within single  
692 cores pointed to consistent coupling with past and present biogeochemical processes.  
693 Altogether, these spatial patterns underline the relevance of a targeted sampling strategy to  
694 resolve geochemical heterogeneities in the shallow subseafloor, which proves essential for  
695 capturing the transient nature of seepage. Fine-scale geochemical variations are easily  
696 overlooked but are nonetheless crucial for understanding seep dynamics and differentiating  
697 between active and past seepage processes, requiring adequate spatial and temporal  
698 coverage and geostatistical techniques.

## 699 **6. Data availability**

700 The geochemical data is available on PANGAEA as dataset #974341 and #974346 under  
701 digital object identifier <https://doi.pangaea.de/10.1594/PANGAEA.974341> and  
702 <https://doi.pangaea.de/10.1594/PANGAEA.974346>.

## 703 **7. Author contributions**

704 JK and RDP organized the sampling cruise. ES and JK designed the study and collected  
705 samples. ES performed cell counts and analyzed pore water geochemistry under the  
706 supervision of JK. XRF measurements were performed under the supervision of JS. FT-ICR-  
707 MS analyses of organic extracts were carried out by KM and SP. ES analyzed the data in  
708 collaboration with AV, JK and SP. ES wrote the manuscript with input and revisions from all  
709 co-authors.

## 710 **8. Competing interests**

711 The authors declare that they have no conflict of interest.

## 712 **9. Acknowledgements**

713 We thank all crew members of the RV *Sverdrup II*, Steffen Okolski, J. Axel Kitte and Edgar  
714 Kutschera for their great help during the sampling cruise. The help of Steffen Okolski in pore  
715 water analyses is acknowledged. We acknowledge the support of Anja Schleicher, Andrea  
716 Gottsche and Heike Rothe in performing the XRF and ICP-MS measurements, including  
717 sample melting and instrument operation. Sabine Kasten and Bo Liu are thanked for advices  
718 on data processing.

## 719 **10. Financial support**

720 This research has received funding from the European Union's Horizon 2020 research and  
721 innovation programme under grant agreement no. 899667. The article processing charge for  
722 this open-access publication were covered by GFZ Helmholtz Centre for Geosciences.

723

724 The PROSPECTOMICS Consortium

725 The principal investigators of the PROSPECTOMICS project are Jens Kallmeyer<sup>1</sup>, Paul  
726 Wilmes<sup>2</sup>, Alexander J. Probst<sup>3</sup>, Dörte Becher<sup>4</sup>, Thomas Rattai<sup>5</sup>, and Rolando di Primio<sup>6</sup>. The  
727 project managers are Aurèle Vuillemin<sup>1</sup>, Cédric L. Laczny<sup>2</sup>, André R. Soares<sup>3</sup>, and Anke  
728 Trautwein-Schult<sup>4</sup>. Scientists and technicians include Ellen Schnabel<sup>1</sup>, Kai Mangelsdorf<sup>7</sup>,  
729 Steffen Okolski<sup>1</sup>, J. Axel Kitte<sup>1</sup>, Benoit Kunath<sup>2</sup>, Zainab Zafar<sup>2</sup>, Sarah Esser<sup>3</sup>, Anne Ostrzinski<sup>4</sup>,  
730 Sebastian Grund<sup>4</sup>, and Alexander Pfundner<sup>5</sup>.

731 <sup>1</sup>GFZ Helmholtz Centre for Geosciences, Section Geomicrobiology, Telegrafenberg, 14473  
732 Potsdam, Germany; <sup>2</sup>Luxembourg Centre for Systems Biomedicine, University of  
733 Luxembourg, Esch-sur-Alzette; <sup>3</sup>Environmental Metagenomics, Research Center One Health  
734 Ruhr of the University Alliance Ruhr, Faculty of Chemistry, University of Duisburg-Essen,  
735 Essen, Germany; <sup>4</sup>Department of Microbial Proteomics, University of Greifswald, Greifswald,  
736 Germany; <sup>5</sup>Computational Systems Biology, Centre for Microbiology and Environmental  
737 Systems Science, University of Vienna, Vienna, Austria; <sup>6</sup>Aker BP ASA, Sandvika, Viken,

738 Norway; <sup>7</sup>GFZ Helmholtz Centre for Geosciences, Section, Section Organic Geochemistry,  
739 Telegrafenberg, 14473 Potsdam, Germany.

## 740 **11. References**

741 Abrams, M. A.: Significance of hydrocarbon seepage relative to petroleum generation and  
742 entrapment, *Marine and Petroleum Geology*, 22, 457-477,  
743 <https://doi.org/10.1016/j.marpetgeo.2004.08.003>, 2005.

744 Abrams, M. A.: Marine seepage variability and its impact on evaluating the surface migrated  
745 hydrocarbon seep signal, *Marine and Petroleum Geology*, 121, 13,  
746 <https://doi.org/10.1016/j.marpetgeo.2020.104600>, 2020.

747 Alkhatib, M., Qutob, M., Alkhatib, S., and Eisenhauer, A.: Influence of precipitation rate and  
748 temperature on the partitioning of magnesium and strontium in calcite overgrowths,  
749 *Chemical Geology*, 599, <https://doi.org/10.1016/j.chemgeo.2022.120841>, 2022.

750 Andreassen, K., Laberg, J. S., and Vorren, T. O.: Seafloor geomorphology of the SW Barents  
751 Sea and its glaci-dynamic implications, *Geomorphology*, 97, 157-177,  
752 <https://doi.org/10.1016/j.geomorph.2007.02.050>, 2008.

753 Argentino, C., Waghorn, K. A., Vadakkepuliambatta, S., Polteau, S., Bunz, S., and Panieri, G.:  
754 Dynamic and history of methane seepage in the SW Barents Sea: new insights from  
755 Leirdjupet Fault Complex, *Sci Rep*, 11, 4373, <https://doi.org/10.1038/s41598-021-83542-0>,  
756 2021.

757 Bach, L. T.: The additionality problem of ocean alkalinity enhancement, *Biogeosciences*, 21,  
758 261-277, <https://doi.org/10.5194/bg-21-261-2024>, 2024.

759 Berner, R. A.: A new geochemical classification of sedimentary environments, *Journal of*  
760 *Sedimentary Research*, 51, 359-365, [https://doi.org/10.1306/212f7c7f-2b24-11d7-](https://doi.org/10.1306/212f7c7f-2b24-11d7-8648000102c1865d)  
761 [8648000102c1865d](https://doi.org/10.1306/212f7c7f-2b24-11d7-8648000102c1865d), 1981.

762 Bowles, M. W., Mogollon, J. M., Kasten, S., Zabel, M., and Hinrichs, K. U.: Global rates of  
763 marine sulfate reduction and implications for sub-sea-floor metabolic activities, *Science*,  
764 344, 889-891, <https://doi.org/10.1126/science.1249213>, 2014.

765 Bradley, J. A., Arndt, S., Amend, J. P., Burwicz, E., Dale, A. W., Egger, M., and LaRowe, D. E.:  
766 Widespread energy limitation to life in global subseafloor sediments, *Sci Adv*, 6, eaba0697,  
767 <https://doi.org/10.1126/sciadv.aba0697>, 2020.

768 Brown, M. B. and Forsythe, A. B.: Robust Tests for the Equality of Variances, *Journal of the*  
769 *American Statistical Association*, 69, 364-367,  
770 <https://doi.org/10.1080/01621459.1974.10482955>, 1974.

- 771 Carter, S. C., Paytan, A., and Griffith, E. M.: Toward an Improved Understanding of the  
 772 Marine Barium Cycle and the Application of Marine Barite as a Paleoproductivity Proxy,  
 773 *Minerals*, 10, <https://doi.org/10.3390/min10050421>, 2020.
- 774 Chavez, F. P., Messié, M., and Pennington, J. T.: Marine primary production in relation to  
 775 climate variability and change, *Annual Review of Marine Science*, 3, 227–260,  
 776 <https://doi.org/10.1146/annurev.marine.010908.163917>, 2011.
- 777 Ciotoli, G., Procesi, M., Etiope, G., Fracassi, U., and Ventura, G.: Influence of tectonics on  
 778 global scale distribution of geological methane emissions, *Nat Commun*, 11, 2305,  
 779 <https://doi.org/10.1038/s41467-020-16229-1>, 2020.
- 780 Cline, J. D.: Spectrophotometric Determination of Hydrogen Sulfide in Natural Waters<sup>1</sup>,  
 781 *Limnol Oceanogr*, 14, 454-458, <https://doi.org/10.4319/lo.1969.14.3.0454>, 1969.
- 782 Dale, A. W., Aguilera, D. R., Regnier, P., Fossing, H., Knab, N. J., and Jorgensen, B. B.:  
 783 Seasonal dynamics of the depth and rate of anaerobic oxidation of methane in Aarhus Bay  
 784 (Denmark) sediments, *Journal of Marine Research*, 66, 127-155,  
 785 <https://doi.org/10.1357/002224008784815775>, 2008.
- 786 de Groot, T. R., Kalenitchenko, D., Moser, M., Argentino, C., Panieri, G., Lindgren, M.,  
 787 Dølven, K. O., Ferré, B., Svenning, M. M., and Niemann, H.: Methanotroph activity and  
 788 connectivity between two seep systems north off Svalbard, *Frontiers in Earth Science*, 12,  
 789 <https://doi.org/10.3389/feart.2024.1287226>, 2024.
- 790 Dong, H., Jaisi, D. P., Kim, J., and Zhang, G.: Microbe-clay mineral interactions, *American*  
 791 *Mineralogist*, 94, 1505-1519, <https://doi.org/10.2138/am.2009.3246>, 2009.
- 792 Doré, A. G.: Barents Sea Geology, Petroleum Resources and Commercial Potencial, *ARCTIC*,  
 793 48, 207-221, 1995.
- 794 Edenborn, H. M., Paquin, Y., and Chateauneuf, G.: Bacterial contribution to manganese  
 795 oxidation in a deep coastal sediment, *Estuarine, Coastal and Shelf Science*, 21, 801-815,  
 796 [https://doi.org/10.1016/0272-7714\(85\)90074-5](https://doi.org/10.1016/0272-7714(85)90074-5), 1985.
- 797 Eichhubl, P., Davatzes, N. C., and Becker, S. P.: Structural and diagenetic control of fluid  
 798 migration and cementation along the Moab fault, Utah, *Aapg Bulletin*, 93, 653-681,  
 799 <https://doi.org/10.1306/02180908080>, 2009.
- 800 Elverhøi, A. and Solheim, A.: The Barents Sea ice sheet - a sedimentological discussion, *Polar*  
 801 *Research*, 1, 23-42, <https://doi.org/10.1111/j.1751-8369.1983.tb00729.x>, 1983.
- 802 Elverhøi, A., Fjeldskaar, W., Solheim, A., Nyland-Berg, M., and Russwurm, L.: The Barents Sea  
 803 Ice Sheet - a model of its growth and decay during the last ice maximum, *Quaternary*  
 804 *Science Reviews*, 12, 11, [https://doi.org/10.1016/0277-3791\(93\)90025-H](https://doi.org/10.1016/0277-3791(93)90025-H), 1993.
- 805 Etiope, G.: *Natural Gas Seepage- The Earth's Hydrocarbon Degassing*, Springer, ISBN 978-3-  
 806 319-14601-0, 2015.

- 807 Faleide, J. I., Gudlaugsson, S. T., and Jacquart, G.: Evolution of the western Barents Sea,  
 808 Marine and Petroleum Geology, 1, 123-150, [https://doi.org/10.1016/0264-8172\(84\)90082-](https://doi.org/10.1016/0264-8172(84)90082-5)  
 809 5, 1984.
- 810 Fischer, D., Sahling, H., Nöthen, K., Bohrmann, G., Zabel, M., and Kasten, S.: Interaction  
 811 between hydrocarbon seepage, chemosynthetic communities, and bottom water redox at  
 812 cold seeps of the Makran accretionary prism: insights from habitat-specific pore water  
 813 sampling and modeling, Biogeosciences, 9, 2013-2031, [https://doi.org/10.5194/bg-9-2013-](https://doi.org/10.5194/bg-9-2013-814)  
 814 2012, 2012.
- 815 Foster, K. L., Stern, G. A., Carrie, J., Bailey, J. N., Outridge, P. M., Sanei, H., and Macdonald, R.  
 816 W.: Spatial, temporal, and source variations of hydrocarbons in marine sediments from  
 817 Baffin Bay, Eastern Canadian Arctic, Sci Total Environ, 506-507, 430-443,  
 818 <https://doi.org/10.1016/j.scitotenv.2014.11.002>, 2015.
- 819 Froelich, P. N., Klinkhammer, G. P., Bender, M. L., Luedtke, N. A., Heath, G. R., Cullen, D.,  
 820 Dauphin, P., Hammond, D., Hartman, B., and Maynard, V.: Early oxidation of organic matter  
 821 in pelagic sediments of the eastern equatorial Atlantic: suboxic diagenesis, Geochimica et  
 822 Cosmochimica Acta, 43, 1975-1090, [https://doi.org/10.16/0016-7037\(79\)90095-4](https://doi.org/10.16/0016-7037(79)90095-4), 1979.
- 823 Gabrielsen, R. H., Faerseth, R. B., Jensen, L. N., Kalheim, J. E., and Riis, F.: Structural elements  
 824 of the Norwegian continental shelf, Part 1: The Barents Sea Region, NPD Bulletin, 6, 1-33,  
 825 1990.
- 826 Heggland, R.: Gas seepage as an indicator of deeper prospective reservoirs. A study based  
 827 on exploration 3D seismic data, Marine and Petroleum Geology, 15, 1-9,  
 828 [https://doi.org/10.1016/S0264-8172\(97\)00060-3](https://doi.org/10.1016/S0264-8172(97)00060-3), 1998.
- 829 Hinrichs, K. U., Hayes, J. M., Sylva, S. P., Brewer, P. G., and DeLong, E. F.: Methane-  
 830 consuming archaeobacteria in marine sediments, Nature, 398, 802-805,  
 831 <https://doi.org/10.1038/19751>, 1999.
- 832 Hoareau, G., Monnin, C., and Odonne, F.: A study of celestine equilibrium in marine  
 833 sediments using the entire ODP/IODP porewater data base, Geochimica et Cosmochimica  
 834 Acta, 74, 3925-3937, <https://doi.org/10.1016/j.gca.2010.03.033>, 2010.
- 835 Hu, L., Yvon-Lewis, S. A., Kessler, J. D., and MacDonald, I. R.: Methane fluxes to the  
 836 atmosphere from deepwater hydrocarbon seeps in the northern Gulf of Mexico, Journal of  
 837 Geophysical Research: Oceans, 117, <https://doi.org/10.1029/2011jc007208>, 2012.
- 838 Hu, T., Luo, M., Qi, Y., He, D., Chen, L., Xu, Y., and Chen, D.: Molecular evidence for the  
 839 production of labile, sulfur-bearing dissolved organic matter in the seep sediments of the  
 840 South China Sea, Water Res, 233, 119732, <https://doi.org/10.1016/j.watres.2023.119732>,  
 841 2023.
- 842 Huerta-Diaz, M. A. and Morse, J. W.: Pyritization of trace metals in anoxic marine sediments,  
 843 Geochimica et Cosmochimica Acta, 56, 2681-2702, [https://doi.org/10.1016/0016-](https://doi.org/10.1016/0016-7037(92)90353-k)  
 844 7037(92)90353-k, 1992.

- 845 Hunt, J. M.: *Petroleum Geochemistry and Geology*, W.H.Freeman & Co Ltd, New York, ISBN  
846 9780716724414, 1995.
- 847 Hvoslef, S., Christie, O. H. J., Sassen, R., Kennicutt, M. C., Requejo, A. G., and Brooks, J. M.:  
848 Test of a new surface geochemistry tool for resource prediction in frontier areas, *Marine*  
849 *and Petroleum Geology*, 13, 107-124, [https://doi.org/10.1016/0264-8172\(95\)00032-1](https://doi.org/10.1016/0264-8172(95)00032-1), 1996.
- 850 Iversen, N. and Jørgensen, B. B.: Diffusion coefficients of sulfate and methane in marine  
851 sediments: Influence of porosity, *Geochemica et Cosmochemica Acta*, 57, 571-778,  
852 [https://doi.org/10.1016/0016-7037\(93\)90368-7](https://doi.org/10.1016/0016-7037(93)90368-7), 1993.
- 853 Johansen, S. E., Ostist, B. K., Birkeland, Ø., Fedorovsky, Y. F., Martirosjan, V. N., Bruun  
854 Christensen, O., Cheredeev, S. I., Ignatenko, E. A., and Margulis, L. S.: Hydrocarbon potential  
855 in the Barents Sea region: play distribution and potential, *Norwegian Petroleum Society*  
856 *Special Publications*, 2, 273-320, <https://doi.org/10.1016/B978-0-444-88943-0.50024-1>,  
857 1993.
- 858 Jørgensen, B. B.: Mineralization of organic matter in the sea bed—the role of sulphate  
859 reduction, *Nature*, 296, 643-645, <https://doi.org/10.1038/296643a0>, 1982.
- 860 Jørgensen, B. B. and Kasten, S.: Sulfur Cycling and Methane Oxidation, in: *Marine*  
861 *Geochemistry*, 271-309, [https://doi.org/10.1007/3-540-32144-6\\_8](https://doi.org/10.1007/3-540-32144-6_8), 2006.
- 862 Jørgensen, B. B., Findlay, A. J., and Pellerin, A.: The Biogeochemical Sulfur Cycle of Marine  
863 Sediments, *Front Microbiol*, 10, 849, <https://doi.org/10.3389/fmicb.2019.00849>, 2019.
- 864 Joye, S. B.: The Geology and Biogeochemistry of Hydrocarbon Seeps, *Annual Review of Earth*  
865 *and Planetary Sciences*, 48, 205-231, [https://doi.org/10.1146/annurev-earth-063016-](https://doi.org/10.1146/annurev-earth-063016-020052)  
866 [020052](https://doi.org/10.1146/annurev-earth-063016-020052), 2020.
- 867 Joye, S. B., Bowles, M. W., and Ziervogel, K.: Marine Biogeochemical Cycles, in: *The Marine*  
868 *Microbiome*, 623-671, [https://doi.org/10.1007/978-3-030-90383-1\\_15](https://doi.org/10.1007/978-3-030-90383-1_15), 2022.
- 869 Joye, S. B., Boetius, A., Orcutt, B. N., Montoya, J. P., Schulz, H. N., Erickson, M. J., and Lugo,  
870 S. K.: The anaerobic oxidation of methane and sulfate reduction in sediments from Gulf of  
871 Mexico cold seeps, *Chemical Geology*, 205, 219-238,  
872 <https://doi.org/10.1016/j.chemgeo.2003.12.019>, 2004.
- 873 Judd, A. and Hovland, M.: *Seabed fluid flow- The impact on geology, biology and the marine*  
874 *environment*, Cambridge University Press, <https://doi.org/10.1017/cbo9780511535918>,  
875 2009.
- 876 Kallmeyer, J., Smith, D. C., Spivack, A. J., and D'Hondt, S.: New cell extraction procedure  
877 applied to deep subsurface sediments, *Limnology and Oceanography: Methods*, 6, 236-245,  
878 <https://doi.org/10.4319/lom.2008.6.236>, 2008.
- 879 Karaca, D., Hensen, C., and Wallmann, K.: Controls on authigenic carbonate precipitation at  
880 cold seeps along the convergent margin off Costa Rica, *Geochemistry, Geophysics,*  
881 *Geosystems*, 11, <https://doi.org/10.1029/2010gc003062>, 2010.

- 882 Kars, M. A. C., Pastor, L., Burin, C., and Koornneef, L. M. T.: Data report: characterization of  
 883 iron oxides and iron sulfides in sediments from IODP Expedition 385 Sites U1549 and U1552  
 884 using rock magnetism and geochemistry, in: Proceedings of the International Ocean  
 885 Discovery Program, Teske, A., Lizarralde, D., Höfig, T. W., and the Expedition 385 Scientists  
 886 (Eds.), Volume 385, 19 pp., International Ocean Discovery Program,  
 887 <https://doi.org/10.14379/iodp.proc.385.207.2025>, 2025.
- 888 Kasten, S. and Jørgensen, B. B.: Sulfate Reduction in Marine Sediments, in: Marine  
 889 Geochemistry, Springer, Heidelberg, 263-281, [https://doi.org/10.1007/978-3-662-04242-](https://doi.org/10.1007/978-3-662-04242-7_8)  
 890 [7\\_8](https://doi.org/10.1007/978-3-662-04242-7_8), 2000.
- 891 Kim, J., Dong, H. L., Seabaugh, J., Newell, S. W., and Eberl, D. D.: Role of microbes in the  
 892 smectite-to-illite reaction, *Science*, 303, 830-832, <https://doi.org/10.1126/science.1093245>,  
 893 2004.
- 894 Knies, J. and Martinez, P.: Organic matter sedimentation in the western Barents Sea region:  
 895 Terrestrial and marine contribution based on isotopic composition and organic nitrogen  
 896 content, *Norwegian Journal of Geology*, 89, 79-89, 2009.
- 897 Knight, A. W., Harvey, J. A., Shohel, M., Lu, P., Cummings, D., and Ilgen, A. G.: The combined  
 898 effects of Mg<sup>2+</sup> and Sr<sup>2+</sup> incorporation during CaCO<sub>3</sub> precipitation and crystal growth,  
 899 *Geochimica et Cosmochimica Acta*, 345, 16-33, <https://doi.org/10.1016/j.gca.2023.01.021>,  
 900 2023.
- 901 Langrock, U., Stein, R., Lipinski, M., and Brumsack, H.-J. r.: Paleoenvironment and sea-level  
 902 change in the early Cretaceous Barents Sea?implications from near-shore marine sapropels,  
 903 *Geo-Marine Letters*, 23, 34-42, <https://doi.org/10.1007/s00367-003-0122-5>, 2003.
- 904 Larssen, G. B., Elvebakk, G., Henriksen, L. B., Kristensen, S.-E., Nilsson, I., Samuelsen, T. J.,  
 905 Svana, T. A., Stemmerik, L., and Worsley, D.: Upper Palaeozoic lithostratigraphy of the  
 906 Southern Norwegian Barents Sea, *Norsk Geologisk Undersøkelser, Bull.*, 444, 43, 2002.
- 907 Leifer, I., Boles, J. R., Luyendyk, B. P., and Clark, J. F.: Transient discharges from marine  
 908 hydrocarbon seeps: spatial and temporal variability, *Environmental Geology*, 46, 1038-1052,  
 909 <https://doi.org/10.1007/s00254-004-1091-3>, 2004.
- 910 Lin, Z., Sun, X., Peckmann, J., Lu, Y., Xu, L., Strauss, H., Zhou, H., Gong, J., Lu, H., and Teichert,  
 911 B. M. A.: How sulfate-driven anaerobic oxidation of methane affects the sulfur isotopic  
 912 composition of pyrite: A SIMS study from the South China Sea, *Chemical Geology*, 440, 26-  
 913 41, <https://doi.org/10.1016/j.chemgeo.2016.07.007>, 2016.
- 914 Mann, H. B. and Whitney, D. R.: On a Test of Whether one of Two Random Variables is  
 915 Stochastically Larger than the Other, *The Annals of Mathematical Statistics*, 18, 50-60,  
 916 <https://doi.org/10.1214/aoms/1177730491>, 1947.
- 917 Marín, D., Hølleren, S., Escalona, A., Olausson, S., Cedeño, A., Nøhr-Hansen, H., and Ohm, S.:  
 918 The Middle Jurassic to lowermost Cretaceous in the SW Barents Sea: Interplay between

- 919 tectonics, coarse-grained sediment supply and organic matter preservation, *Basin Research*,  
 920 33, 1033-1055, <https://doi.org/10.1111/bre.12504>, 2020.
- 921 Marshall, A. G. and Rodgers, R. P.: Petroleomics: the next grand challenge for chemical  
 922 analysis, *Acc Chem Res*, 37, 53-59, <https://doi.org/10.1021/ar020177t>, 2004.
- 923 Matheron, G.: Principles of geostatistics, *Economic Geology*, 58, 1246-1266,  
 924 <https://doi.org/10.2113/gsecongeo.58.8.1246>, 1963.
- 925 Miao, X., Feng, X., Li, J., Liu, X., Liang, J., Feng, J., Xiao, Q., Dan, X., and Wei, J.: Enrichment  
 926 mechanism of trace elements in pyrite under methane seepage, *Geochemical Perspectives  
 927 Letters*, 21, 18-22, <https://doi.org/10.7185/geochemlet.2211>, 2022.
- 928 Middelburg, J. J.: Reviews and syntheses: to the bottom of carbon processing at the  
 929 seafloor, *Biogeosciences*, 15, 413-427, <https://doi.org/10.5194/bg-15-413-2018>, 2018.
- 930 Nickel, J. C., di Primio, R., Mangelsdorf, K., Stoddart, D., and Kallmeyer, J.: Characterization  
 931 of microbial activity in pockmark fields of the SW-Barents Sea, *Marine Geology*, 332-334,  
 932 152-162, <https://doi.org/10.1016/j.margeo.2012.02.002>, 2012.
- 933 Nickel, J. C., di Primio, R., Kallmeyer, J., Hammer, Ø., Horsfield, B., Stoddart, D., Brunstad, H.,  
 934 and Mangelsdorf, K.: Tracing the origin of thermogenic hydrocarbon signals in pockmarks  
 935 from the southwestern Barents Sea, *Organic Geochemistry*, 63, 73-84,  
 936 <https://doi.org/10.1016/j.orggeochem.2013.08.008>, 2013.
- 937 Orphan, V. J., Hinrichs, K. U., Ussler, W., 3rd, Paull, C. K., Taylor, L. T., Sylva, S. P., Hayes, J.  
 938 M., and Delong, E. F.: Comparative analysis of methane-oxidizing archaea and sulfate-  
 939 reducing bacteria in anoxic marine sediments, *Appl Environ Microbiol*, 67, 1922-1934,  
 940 <https://doi.org/10.1128/AEM.67.4.1922-1934.2001>, 2001.
- 941 Padilla, A. M., Loranger, S., Kinnaman, F. S., Valentine, D. L., and Weber, T. C.: Modern  
 942 Assessment of Natural Hydrocarbon Gas Flux at the Coal Oil Point Seep Field, Santa Barbara,  
 943 California, *Journal of Geophysical Research: Oceans*, 124, 2472-2484,  
 944 <https://doi.org/10.1029/2018jc014573>, 2019.
- 945 Pearson, K.: Note on regression and inheritance in the case of two parents, *Proceedings of  
 946 the Royal Society of London*, 58, 240-242, <https://doi.org/10.1098/rspl.1895.0041>, 1895.
- 947 Pebesma, E. J.: Multivariable geostatistics in S: the gstat package, *Computers & Geosciences*,  
 948 30, 683-691, <https://doi.org/10.1016/j.cageo.2004.03.012>, 2004.
- 949 Peckmann, J., Reimer, A., Luth, U., Luth, C., Hansen, B. T., Heinicke, C., Hoefs, J., and Reitner,  
 950 J.: Methane-derived carbonates and authigenic pyrite from the northwestern Black Sea,  
 951 *Marine Geology*, 177, 129-150, [https://doi.org/10.1016/S0025-3227\(01\)00128-1](https://doi.org/10.1016/S0025-3227(01)00128-1), 2001.
- 952 Poetz, S., Horsfield, B., and Wilkes, H.: Maturity-Driven Generation and Transformation of  
 953 Acidic Compounds in the Organic-Rich Posidonia Shale as Revealed by Electrospray  
 954 Ionization Fourier Transform Ion Cyclotron Resonance Mass Spectrometry, *Energy & Fuels*,  
 955 28, 4877-4888, <https://doi.org/10.1021/ef500688s>, 2014.

- 956 Pop Ristova, P., Wenzhofer, F., Ramette, A., Felden, J., and Boetius, A.: Spatial scales of  
 957 bacterial community diversity at cold seeps (Eastern Mediterranean Sea), *ISME J*, 9, 1306-  
 958 1318, <https://doi.org/10.1038/ismej.2014.217>, 2015.
- 959 R: A language and environment for statistical computing: <https://www.R-project.org/>, last  
 960 access: 2023-06-12.
- 961 Radovic, J. R. and Silva, R. C.: Ultrahigh-Resolution Mass Spectrometry Advances for  
 962 Biogeochemical Analysis: From Seafloor Sediments to Petroleum and Marine Oil Spills, *J Am  
 963 Soc Mass Spectrom*, 36, 7-33, <https://doi.org/10.1021/jasms.4c00266>, 2025.
- 964 Rasheed, M. A., Lakshmi, M., Rao, P. L. S., Kalpana, M. S., Dayal, A. M., and Patil, D. J.:  
 965 Geochemical evidences of trace metal anomalies for finding hydrocarbon microseepage in  
 966 the petroliferous regions of the Tatipaka and Pasarlapudi areas of Krishna Godavari Basin,  
 967 India, *Petroleum Science*, 10, 19-29, <https://doi.org/10.1007/s12182-013-0245-x>, 2013.
- 968 Rovere, M., Mercorella, A., Frapiccini, E., Funari, V., Spagnoli, F., Pellegrini, C., Bonetti, A. S.,  
 969 Veneruso, T., Tassetti, A. N., Dell'Orso, M., Mastroianni, M., Giuliani, G., De Marco, R., Fabi,  
 970 G., Ciccone, F., and Antoncecchi, I.: Geochemical and Geophysical Monitoring of  
 971 Hydrocarbon Seepage in the Adriatic Sea, *Sensors (Basel)*, 20,  
 972 <https://doi.org/10.3390/s20051504>, 2020.
- 973 Røy, H., Kallmeyer, J., Adhikari, R. R., Pockalny, R., Jørgensen, B. B., and D'Hondt, S.: Aerobic  
 974 microbial respiration in 86-million-year-old deep-sea red clay, *Science*, 336, 922-925,  
 975 <https://doi.org/10.1126/science.1219424>, 2012.
- 976 Sættem, J., Rise, L., and Westgaard, D. A.: Composition and properties of glacial  
 977 sediments in the southwestern Barents Sea, *Marine Geotechnology*, 10, 229-255,  
 978 <https://doi.org/10.1080/10641199109379893>, 1991.
- 979 Schippers, A. and Jørgensen, B. B.: Oxidation of pyrite and iron sulfide by manganese dioxide  
 980 in marine sediments, *Geochimica et Cosmochimica Acta*, 65, 915-922,  
 981 [https://doi.org/10.1016/s0016-7037\(00\)00589-5](https://doi.org/10.1016/s0016-7037(00)00589-5), 2001.
- 982 Schnabel, E., Vuillemin, A., Laczny, C. C., Kunath, B. J., Soares, A. R., Probst, A. J., Di Primio,  
 983 R., Kallmeyer, J., and the, P. C.: Influence of minor hydrocarbon seepage on sulfur cycling in  
 984 marine subsurface sediments, *Biogeosciences*, 22, 767-784, <https://doi.org/10.5194/bg-22-767-2025>, 2025.
- 986 Schneider, R. R., Schulz, H. D., and Hensen, C.: Marine Carbonates: Their Formation and  
 987 Destruction, in: *Marine Geochemistry*, edited by: Schulz, H. D., and Zabel, M., Springer,  
 988 Berlin, Heidelberg, 311-337, [https://doi.org/10.1007/3-540-32144-6\\_9](https://doi.org/10.1007/3-540-32144-6_9), 2006.
- 989 Schulz, H. D.: Quantification of Early Diagenesis: Dissolved Constituents in Pore Water and  
 990 Signals in the Solid Phase, in: *Marine Geochemistry*, 73-124, [https://doi.org/10.1007/3-540-32144-6\\_3](https://doi.org/10.1007/3-540-32144-6_3), 2006.
- 992 Sedgwick, P.: Pearson's correlation coefficient, *Bmj*, 345, e4483-e4483,  
 993 <https://doi.org/10.1136/bmj.e4483>, 2012.

- 994 Seeberg-Elverfeldt, J., Schluter, M., Feseker, T., and Kolling, M.: Rhizon sampling of  
 995 porewaters near the sediment-water interface of aquatic systems, *Limnol Oceanogr-Meth*,  
 996 3, 361-371, <https://doi.org/10.4319/lom.2005.3.361>, 2005.
- 997 Sert, M. F., D'Andrilli, J., Gründger, F., Niemann, H., Granskog, M. A., Pavlov, A. K., Ferré, B.,  
 998 and Silyakova, A.: Compositional Differences in Dissolved Organic Matter Between Arctic  
 999 Cold Seeps Versus Non-Seep Sites at the Svalbard Continental Margin and the Barents Sea,  
 1000 *Frontiers in Earth Science*, 8, <https://doi.org/10.3389/feart.2020.552731>, 2020.
- 1001 Siegert, M. J., Dowdeswell, J. A., Hald, M., and Svendsen, J. I.: Modelling the Eurasian Ice  
 1002 Sheet through a full (Weichselian) glacial cycle, *Global and Planetary Change*, 31, 367-385,  
 1003 [https://doi.org/10.1016/S0921-8181\(01\)00130-8](https://doi.org/10.1016/S0921-8181(01)00130-8), 2001.
- 1004 Smrzka, D., Lin, Z., Monien, P., Chen, T., Bach, W., Peckmann, J., and Bohrmann, G.: Pyrite-  
 1005 based trace element fingerprints for methane and oil seepage, *Geochemical Perspectives*  
 1006 *Letters*, 29, 33-37, <https://doi.org/10.7185/geochemlet.2409>, 2024.
- 1007 Smrzka, D., Zwicker, J., Bach, W., Feng, D., Himmler, T., Chen, D., and Peckmann, J.: The  
 1008 behavior of trace elements in seawater, sedimentary pore water, and their incorporation  
 1009 into carbonate minerals: a review, *Facies*, 65, 47, [https://doi.org/10.1007/s10347-019-0581-](https://doi.org/10.1007/s10347-019-0581-4)  
 1010 4, 2019.
- 1011 Smrzka, D., Feng, D., Himmler, T., Zwicker, J., Hu, Y., Monien, P., Tribovillard, N., Chen, D.,  
 1012 and Peckmann, J.: Trace elements in methane-seep carbonates: Potentials, limitations, and  
 1013 perspectives, *Earth-Science Reviews*, 208, <https://doi.org/10.1016/j.earscirev.2020.103263>,  
 1014 2020.
- 1015 Tribovillard, N., du Châtelet, E. A., Gay, A., Barbecot, F., Sansjofre, P., and Potdevin, J.-L.:  
 1016 Geochemistry of cold seepage-impacted sediments: Per-ascensum or per-descensum trace  
 1017 metal enrichment?, *Chemical Geology*, 340, 1-12,  
 1018 <https://doi.org/10.1016/j.chemgeo.2012.12.012>, 2013.
- 1019 Viollier, E., Inglett, P. W., Hunter, K., Roychoudhury, A. N., and Van Cappellen, P.: The  
 1020 ferrozine method revisited: Fe(II)/Fe(III) determination in natural waters, *Applied*  
 1021 *Geochemistry*, 15, 785-790, [https://doi.org/10.1016/s0883-2927\(99\)00097-9](https://doi.org/10.1016/s0883-2927(99)00097-9), 2000.
- 1022 von Breyman, M. T., Brumsack, H., and Emeis, K. C.: Depositional and Diagenetic Behavior  
 1023 of Barium in the Japan Sea, in: *Proceedings of the Ocean Drilling Program, 127/128 Part 1*  
 1024 *Scientific Results, Proceedings of the Ocean Drilling Program*,  
 1025 <https://doi.org/10.2973/odp.proc.sr.127128-1.168.1992>, 1992.
- 1026 Vuillemin, A., Morlock, M., Paskin, A., Benning, L. G., Henny, C., Kallmeyer, J., Russell, J. M.,  
 1027 and Vogel, H.: Authigenic minerals reflect microbial control on pore waters in a ferruginous  
 1028 analogue, *Geochemical Perspectives Letters*, 28, 20-26,  
 1029 <https://doi.org/10.7185/geochemlet.2339>, 2023a.

- 1030 Vuillemin, A., Vargas, S., Coskun, O. K., Pockalny, R., Murray, R. W., Smith, D. C., D'Hondt, S.,  
1031 and Orsi, W. D.: Atribacteria Reproducing over Millions of Years in the Atlantic Abyssal  
1032 Subseafloor, *mBio*, 11, <https://doi.org/10.1128/mBio.01937-20>, 2020.
- 1033 Vuillemin, A., Mayr, C., Schuessler, J. A., Friese, A., Bauer, K. W., Lücke, A., Heuer, V. B.,  
1034 Glombitza, C., Henny, C., von Blanckenburg, F., Russell, J. M., Bijaksana, S., Vogel, H., Crowe,  
1035 S. A., and Kallmeyer, J.: A one-million-year isotope record from siderites formed in modern  
1036 ferruginous sediments, *GSA Bulletin*, 135, 504-522, <https://doi.org/10.1130/b36211.1>,  
1037 2023b.
- 1038 Wickham, H.: *ggplot2*, 2, Use R!, Springer-Verlag, New York, 260 pp.,  
1039 <https://doi.org/10.1007/978-3-319-24277-4>, 2016.
- 1040 Widdel, F., Knittel, K., and Galushko, A.: Anaerobic Hydrocarbon- Degrading  
1041 Microorganisms: An Overview, in: *Handbook of Hydrocarbon and Lipid Microbiology*,  
1042 Springer, Berlin, Heidelberg, 1997-2021, <https://doi.org/10.1007/978-3-540-77587-4>, 2010.
- 1043 Yergin, D.: *The Prize: The Epic Quest for Oil, Money & Power*, Free Press, ISBN  
1044 9781847376466, 2009.
- 1045 Zhang, X., Wu, K., Han, Z., Chen, Z., Liu, Z., Sun, Z., Shao, L., Zhao, Z., and Zhou, L.: Microbial  
1046 diversity and biogeochemical cycling potential in deep-sea sediments associated with  
1047 seamount, trench, and cold seep ecosystems, *Front Microbiol*, 13, 1029564,  
1048 <https://doi.org/10.3389/fmicb.2022.1029564>, 2022.
- 1049 Zhao, R. X., Xue, H. T., Lu, S. F., Greenwell, and Erastova, V.: Revealing crucial effects of  
1050 reservoir environment and hydrocarbon fractions on fluid behavior in kaolinite pores, *Chem  
1051 Eng J*, 489, <https://doi.org/10.1016/j.cej.2024.151362>, 2024.